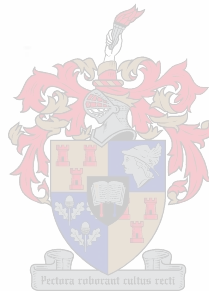


Design of a Passive Rotor Transverse Flux Rotating Machine

By

Duncan Scott Drennan



Thesis presented in partial fulfilment of the requirements for the degree of
Masters of Science in Electrical Engineering at the University of Stellenbosch

Supervisor: Prof. M.J. Kamper

April 2005

Declaration

I, the undersigned, hereby declare that the work contained in this thesis is my own original work and that I have not previously in its entirety or in part submitted it at any university for a degree.

Signature :

Date :

Place :

Abstract

The transverse flux machine (TFM) offers the opportunity of high torque to volume ratios which makes it an excellent candidate for direct wheel drives and low speed generator applications. TFMs have a three dimensional flux path which eliminates iron laminates as a viable core material. Soft magnetic composites have been adopted in these machines due to their isotropic nature. There are three main variants of TFMs, namely, active rotor (with magnets on the rotor), passive rotor (with magnets on the stator), and reluctance (with no magnets). As a relatively recent development in electrical machines, the TFM still has many hurdles facing its adoption in industry. Some of these hurdles are high cogging torque, a difficult construction, and expensive materials.

This thesis focuses on the design of a three phase 50 kW passive rotor machine. Finite element simulation is used to determine the optimal configuration, and the final machine is analysed in detail. The construction process and associated problems are also detailed. The completed machine did not perform to the desired specification, but much knowledge was gleaned about the TFM, the construction caveats, and future potential directions.

Opsomming

Die transversale-vloed masjien (TFM) met sy hoë draaimoment tot volume verhouding, is 'n uitstekende kandidaat vir direkte wiel aandrywing en laë spoed generator toepassings. Die vloedpad van dié masjiene is drie-dimensioneel, wat yster laminasies as kern materiaal elimineer. “Soft magnetic composites” kan gebruik word vir hierdie masjiene as gevolg van hulle isotropiese eienskappe. Daar bestaan drie hoof variante van die TFM, naamlik, die aktiewe rotor (met magnete op die rotor), passiewe rotor (met magnete op to stator), en reluktansie (sonder magnete). Die TFM is 'n redelike nuwe tipe masjien en daar is nog probleme wat opgelos moet word voordat die industrie sal begin om dit te gebruik. Van hierdie probleme is “cogging” draaimoment, 'n moeilike konstruksie en duur materiale.

Die fokus van hierie tesis is op die ontwerp van 'n 50kW drie-fase passiewe rotor masjien. Eindige element simulatie is gebruik om die optimale konfigurasie te kry, en 'n analise is gedoen op die finale masjien. Die konstruksie proses en die probleme wat daarmee saam gaan is ook beskryf. Die prototipe masjien wat gebou is het nie aan sy oorspronklike spesifikasie voldoen nie, maar baie kennis is opgedoen oor die TFM, die konstruksie proses, en potensiële toekomstige toepassings.

Acknowledgements

I would like to thank the following people for the pivotal and supporting roles that they played in the completion of this project,

Prof. Maarten Kamper for his guidance and support

Petro Petzer, André Swart and the workshop staff

Jakkie Blom, Heinie Foot, Jos Weerdenburg and the staff of SMD

Pieter Fick, Andrew Dale and Francios Roussouw

Jon Kerr and GKN Sinter metals

Höganäs AB, Sweden

My parents, Evan and Margaret, for pushing me and helping with the production of this thesis

Contents

1	Introduction		1
1.1	Background		1
1.2	Summary		3
2	Design and Optimisation	<i>To my wife, Donné for supporting and loving me through everything</i>	5
2.1	Introduction		5
2.2	Actuator TDMs	<i>For my God, from whom all things come</i>	5
2.2.1	Low RTDM		5
2.2.2	Low RTDM		8
2.3	Reference TDMs with Dynamic Matrices		9
2.3.1	Formal Migration to C++		9
2.3.2	Formal Migration to C++		11
2.3.3	Formal Migration to C++		11
2.4	Non-linear Control using TDMs		13
2.4.1	Introduction		13
2.4.2	Introduction to Non-linear TDM		15
2.4.3	Non-linear Control using TDMs		17
2.4.4	Non-linear Control using TDMs		17
2.4.5	Non-linear Control using TDMs		20
2.4.6	Non-linear Control using TDMs		20
2.4.7	Non-linear Control using TDMs		24
2.4.8	Non-linear Control using TDMs		25
3	Analysis of Control Systems		27
3.1	Introduction		27
3.2	Control Systems		27
3.2.1	Control Systems		28
3.2.2	Control Systems		28
3.2.3	Control Systems		28
3.2.4	Control Systems		28
3.2.5	Control Systems		28
3.2.6	Control Systems		28
3.2.7	Control Systems		28
3.2.8	Control Systems		28
3.2.9	Control Systems		28
3.2.10	Control Systems		28
3.2.11	Control Systems		28
3.2.12	Control Systems		28
3.2.13	Control Systems		28
3.2.14	Control Systems		28
3.2.15	Control Systems		28
3.2.16	Control Systems		28
3.2.17	Control Systems		28
3.2.18	Control Systems		28
3.2.19	Control Systems		28
3.2.20	Control Systems		28
3.2.21	Control Systems		28
3.2.22	Control Systems		28
3.2.23	Control Systems		28
3.2.24	Control Systems		28
3.2.25	Control Systems		28
3.2.26	Control Systems		28
3.2.27	Control Systems		28
3.2.28	Control Systems		28
3.2.29	Control Systems		28
3.2.30	Control Systems		28
3.2.31	Control Systems		28
3.2.32	Control Systems		28
3.2.33	Control Systems		28
3.2.34	Control Systems		28
3.2.35	Control Systems		28
3.2.36	Control Systems		28
3.2.37	Control Systems		28
3.2.38	Control Systems		28
3.2.39	Control Systems		28
3.2.40	Control Systems		28
3.2.41	Control Systems		28
3.2.42	Control Systems		28
3.2.43	Control Systems		28
3.2.44	Control Systems		28
3.2.45	Control Systems		28
3.2.46	Control Systems		28
3.2.47	Control Systems		28
3.2.48	Control Systems		28
3.2.49	Control Systems		28
3.2.50	Control Systems		28
3.2.51	Control Systems		28
3.2.52	Control Systems		28
3.2.53	Control Systems		28
3.2.54	Control Systems		28
3.2.55	Control Systems		28
3.2.56	Control Systems		28
3.2.57	Control Systems		28
3.2.58	Control Systems		28
3.2.59	Control Systems		28
3.2.60	Control Systems		28
3.2.61	Control Systems		28
3.2.62	Control Systems		28
3.2.63	Control Systems		28
3.2.64	Control Systems		28
3.2.65	Control Systems		28
3.2.66	Control Systems		28
3.2.67	Control Systems		28
3.2.68	Control Systems		28
3.2.69	Control Systems		28
3.2.70	Control Systems		28
3.2.71	Control Systems		28
3.2.72	Control Systems		28
3.2.73	Control Systems		28
3.2.74	Control Systems		28
3.2.75	Control Systems		28
3.2.76	Control Systems		28
3.2.77	Control Systems		28
3.2.78	Control Systems		28
3.2.79	Control Systems		28
3.2.80	Control Systems		28
3.2.81	Control Systems		28
3.2.82	Control Systems		28
3.2.83	Control Systems		28
3.2.84	Control Systems		28
3.2.85	Control Systems		28
3.2.86	Control Systems		28
3.2.87	Control Systems		28
3.2.88	Control Systems		28
3.2.89	Control Systems		28
3.2.90	Control Systems		28
3.2.91	Control Systems		28
3.2.92	Control Systems		28
3.2.93	Control Systems		28
3.2.94	Control Systems		28
3.2.95	Control Systems		28
3.2.96	Control Systems		28
3.2.97	Control Systems		28
3.2.98	Control Systems		28
3.2.99	Control Systems		28
3.2.100	Control Systems		28

Contents

1	Introduction	1
1.1	Background	1
1.2	Summary	3
2	Design and Optimisation	5
2.1	Introduction	5
2.2	Reluctance TFMs	5
2.2.1	C-core RTFM	5
2.2.2	I-core RTFM	8
2.3	Reluctance TFMs with Permanent Magnets	9
2.3.1	Permanent Magnets in Air Gap	9
2.3.2	Permanent Magnets in Core	11
2.3.3	Permanent Magnets as Flux Shields	11
2.4	Active and Passive Rotor TFMs	13
2.4.1	Optimisation	13
2.4.2	U-Core Active Rotor TFM	15
2.4.3	U-core Active Rotor TFM with Flux Concentration	17
2.4.4	C-core Passive Rotor TFM	17
2.4.5	Reduced Magnetic Material Design	20
2.4.6	I-core Passive Rotor TFM	20
2.4.7	U-core Passive Rotor TFM	23
2.5	Summary	25
3	Analysis of Simulation Results	27
3.1	Introduction	27
3.2	Machine Parameters	27
3.2.1	Flux Linkage	28
3.2.2	Back EMF	28
3.2.3	Inductance	29
3.2.4	Resistance	31
3.2.5	Torque Approximation	33

3.3	Multi-phase Torque	34
3.3.1	Cogging Torque	35
3.3.2	Motoring Torque	38
3.3.3	Final Machine Choice	41
4	Heat Management	42
4.1	Introduction	42
4.2	Loss Mechanisms	42
4.3	Simulations	43
5	Construction	49
5.1	Introduction	49
5.2	Construction Process	49
5.2.1	Mechanical Design and Component Manufacturing	49
5.2.2	Rotor Construction	51
5.2.3	Stator Construction	52
5.2.4	Final assembly	54
5.3	Problems Encountered	54
6	Control	59
6.1	Introduction	59
6.2	System Overview	59
6.3	State-space Description	60
6.4	Current Control	61
6.4.1	Design	61
6.4.2	Simulation	63
6.5	Speed Control	64
6.5.1	Design	64
6.5.2	Robust Tracking	66
6.5.3	Simulation	68
6.6	DSP and Machine Effects	68
6.6.1	Machine effects	68
6.6.2	DSP effects	69
6.6.3	Simulations	70
7	Measured Results	76
7.1	Introduction	76
7.2	Limitations to Measurements	76
7.2.1	Removal of Phase B	77
7.2.2	Shorts in Phases A and C to Chassis	77
7.3	Generator Measurements	80

7.3.1	No Load Back EMF	80
7.3.2	Generator Under Load	81
7.4	Motor Measurements	81
7.5	Thermal Measurements	84
8	Conclusions	86
8.1	Summary	86
8.2	Recommendations	87
8.3	Conclusions	88
	References	89
A	Magnetic Data	91
A.1	Somalloy 550 Datasheet	92
A.2	Somalloy 500 BH Curve	96
B	Mechanical Drawings	98
C	Attached CD	110
C.1	Magnetic Data	110
C.2	Magnet Scripts	110
C.3	FE Simulation Data	110
C.4	Mechanical Drawings	110
C.5	Photos	110
C.6	Control System Simulation Code	110
C.7	Control System Simulation Results	110
C.8	DSP Programs	111
C.9	Raw Measurement Data	111
C.10	M-files and Simulink Models	111

List of Figures

1.1	Cross section of transverse flux machine	1
1.2	Cross section of longitudinal flux machine	1
1.3	Double sided TFM with flux concentration [1]	2
1.4	Cross section of double sided TFM with flux concentration [1]	2
1.5	Hasubek's reduced magnet material passive rotor TFM	3
2.1	C-core RTFM FE model	6
2.2	C-core RTFM FE model dimensions (in mm)	6
2.3	2 phase RTFM	6
2.4	3 phase RTFM	6
2.5	3D FE mesh for C-core RTFM	7
2.6	Force curves for C-core RTFM	7
2.7	Extraneous forces acting on C-Core RTFM rotor	8
2.8	I-core RTFM FE model	8
2.9	Force curves for I-core RTFM	9
2.10	C-core RTFM FE model with PMs in air gap	10
2.11	Force curves for C-core RTFM with PMs in air gap	10
2.12	C-core RTFM FE model with PMs in core	11
2.13	Force curves for C-core RTFM with PMs in core	11
2.14	C-core RTFM FE model with PM flux shields	12
2.15	Force curves for C-core RTFM with PM flux shields	12
2.16	Interpolation of three points bracketing a maximum	14
2.17	AR TFM FE model	15
2.18	AR TFM FE model dimensions	15
2.19	Motoring and cogging torque for AR TFM	16
2.20	AR TFM with Flux Concentration FE model	17
2.21	AR TFM with Flux Concentration FE model dimensions	17
2.22	Motoring and cogging torque for AR TFM with flux concentration	18
2.23	C-Core PR TFM FE model	18
2.24	C-Core PR TFM FE model dimensions	18
2.25	Motoring and cogging torque for C-Core PR TFM	19

2.26	Radial force acting on rotor of C-Core PR TFM	19
2.27	RMM PR TFM FE model	20
2.28	RMM PR TFM FE model dimensions	20
2.29	Motoring and cogging torque for RMM PR TFM	21
2.30	Z-directed forces acting on rotor blocks of RMM TFM	21
2.31	I-Core PR TFM FE model	22
2.32	I-Core PR TFM FE model dimensions	22
2.33	Motoring and cogging torque for I-Core PR TFM	22
2.34	Z-directed forces acting on rotor blocks of I-Core TFM	23
2.35	U-Core PR TFM FE model	23
2.36	U-Core PR TFM FE model dimensions	23
2.37	Motoring and cogging torque for U-Core PR TFM	24
3.1	Electrical model of the U-Core PRTFM	28
3.2	Flux linkage vs. position with current as parameter	28
3.3	Flux linkage vs. current with position as a parameter	29
3.4	Back EMF of the machine at 1500 rpm with current as a parameter	30
3.5	Inductance of the machine with current as parameter (steps of 5 A)	30
3.6	L_q with current as a parameter	31
3.7	L_d with current as a parameter	32
3.8	L_0 with current as a parameter	32
3.9	Simulated torque compared to approximated torque	34
3.10	Single phase cogging torque of U-core PRTFM	35
3.11	Two phase cogging torque of U-core PRTFM	36
3.12	Three phase cogging torque of U-core PRTFM	36
3.13	Five phase cogging torque of U-core PRTFM	37
3.14	Cogging torque ripple normalized against single phase ripple	37
3.15	Single phase motoring torque of U-core PRTFM (40 A phase current)	38
3.16	Two phase motoring torque of U-core PRTFM	39
3.17	Three phase motoring torque of U-core PRTFM	39
3.18	Five phase motoring torque of U-core PRTFM	40
3.19	Motoring torque ripple normalized against single phase ripple	40
4.1	Stator Model for Thermodynamic Analysis	43
4.2	Control Volume	43
4.3	Heat flow perpendicular to copper strands	44
4.4	Heat flow parallel to copper strands	44
4.5	Heat sink fins	46
4.6	Temperature for one control volume	48

LIST OF FIGURES

5.1	SMC cylinders used to machine components	50
5.2	Stator SMC block outline and dimensions	50
5.3	Rotor SMC block outline and dimensions	50
5.4	Stator magnet outline and dimensions	50
5.5	SMC and magnet components	51
5.6	Assembling the rotor	52
5.7	Completed rotor assembly	53
5.8	Stator frame with SMC blocks and coil inserted	53
5.9	Inserting the magnets into the stator	54
5.10	Stator of one phase after casting	55
5.11	Completed stator assembly	55
5.12	Completed stator assembly	56
5.13	Completed machine	56
5.14	Completed machine	57
5.15	Skimming the rotor before inserting into the stator	58
6.1	Control system overview	60
6.2	System diagram of a single phase machine	61
6.3	Block diagram for current control	62
6.4	Step response for current control	64
6.5	Block diagram for simplified speed control of a three phase machine	65
6.6	Step response for speed control	66
6.7	Robust control block diagram	68
6.8	Step response for robust speed control ($T_L = 100 Nm$)	69
6.9	Current control with current inversion every 180°_{elec}	70
6.10	Speed under current control with current inversion every 180°_{elec}	71
6.11	Current control with back EMF (no decoupling voltage added)	72
6.12	Speed under current control with back EMF (no decoupling voltage added)	72
6.13	Machine effects influence on speed control ($n_{ref} = 1000 rpm$)	73
6.14	Speed control including quantization and sampling effects ($n_{ref} = 1000 rpm$)	73
6.15	Continuous speed control vs. digital speed control ($n_{ref} = 1000 rpm$)	74
6.16	Complete block diagram for speed control of a three phase machine	75
7.1	Measurement setup	77
7.2	Expected cogging torque	78
7.3	Expected motoring torque	78
7.4	Model of the measured winding resistances	79
7.5	Model to determine point of winding damage	79
7.6	Predicted vs. measured peak no load back EMF	80
7.7	No load back EMF at 30 rpm	81

LIST OF FIGURES

7.8	No load back EMF at 1500 rpm	82
7.9	Phase A voltage, Phase A and C currents at 60 rpm	82
7.10	Phase A voltage and current at 1500 rpm	83
7.11	Alignment of firing angle	84
7.12	Open loop control voltage and current at 360 rpm	85
7.13	Temperature measurements	85
A.1	Somalloy 500 BH Curve	96
B.1	Complete Machine	99
B.2	Machine Components	100
B.3	One Phase	101
B.4	Rotor	102
B.5	Shaft	103
B.6	End Plate	104
B.7	Mounting	105
B.8	Fan and Resolver Plate	106
B.9	Fan Housing	107
B.10	Stator Mould	108
B.11	Coil Former	109

List of Tables

2.1	General symbols for dimensions of active and passive rotor TFMs	15
2.2	Optimised dimensions for the U-Core AR TFM	16
2.3	Optimised dimensions for the U-Core AR TFM with flux concentration	17
2.4	Optimised dimensions for the C-Core PR TFM	18
2.5	Optimised dimensions for the RMM PR TFM	20
2.6	Optimised dimensions for the I-Core PR TFM	20
2.7	Optimised dimensions for the U-Core PR TFM	24
2.8	Comparison of different active and passive rotor TFMs	25
2.9	Material densities	25
4.1	Material Properties for Thermal Simulation	45
4.2	Heat sink parameters	47
7.1	Winding resistance measurements	77
7.2	Model winding resistances	79
A.1	BH Data for Somalloy 500	97

List of Symbols

α	Void factor
δ	Skin depth
λ	Flux linkage
μ	Permittivity
ν_f	Fin efficiency
ω	Frequency
ω_e	Electrical speed
ω_m	Mechanical speed
ρ	Density
σ	Conductivity
θ	Position (degrees/radians)
A	Area
A_{Cu}	Cross section of copper
A_w	Cross sectional area of wire
B	Damping factor
C	Specific heat capacity
c_x	Constant
D_h	Equivalent diameter
e	Back EMF
f	Fill factor
h, k	Heat transfer coefficient
H_{Cu}	Copper height
H_P	Pole height
H_R	Rotor height
H_T	Rotor tooth height (as percentahe of H_R)
I, i	Current
J	Inertia
K	State space gains
K_e	Flux linkage constant
$K_{e_{dc}}$	Flux linkage DC offset
K_S	Park transform matrix

K_T	Torque constant
L	Inductance
L'	Approximate inductance
L_P	Pole length
l_w	Length of wire
M	Magnet height (as percentage of H_R)
N	Number of windings
n	Speed (rpm)
\overline{N}_C	Current control constant
N_p	Number of phases
Nm	Newton meters
\overline{N}_s	Speed control constant
Nu_h	Nusselt number
P	Number of poles
$P_{Cu_{loss}}$	Copper losses
$P_{SMC_{loss}}$	Soft magnetic composite losses
\dot{Q}	Heat flow
\dot{Q}'''	Generated heat
r	Resistance
R_{Cu}	Copper resistance
Re_h	Renold's number
R_T	Thermal resistance
r_{mean}	Mean radius
S	Stator length (as percentage of L_P)
T	Torque
\overline{T}	Average torque
T	Temperature
T_L	Load torque
T_m	Motoring torque
u	Control signal
u_c	Overall heat transfer coefficient
u_{ss}	Steady state control signal
v	Voltage
W_{Cu}	Copper width
W_P	Pole width
W_{Yoke}	Yoke width

Chapter 1

Introduction

1.1 Background

In 1988 Herbert Weh introduced the transverse flux machine (TFM) [1]. This machine has a simple ring winding arranged along its perimeter and employs permanent magnets on the rotor. Fig. 1.1 [1] shows the cross section and flux path of a simple TFM. The core elements are arranged in such a way that the flux flows transversal to the direction of force on the rotor.

Most conventional electrical machines have a longitudinal flux path, i.e. the flux flows in a two dimensional plane perpendicular to the machine's shaft. As can be seen in Fig. 1.2, this leads to a coupling of the space requirements of the windings and the core material. If an increase in the cross-sectional area of the core material is desired, the copper area is reduced and therefore, for constant current loading (i.e. constant amperes per meter air gap), the copper losses increase. Conversely, if an increase in the current loading is desired, and the copper losses are kept constant, there is a reduction in the cross-sectional area of the core material. If an increase in the number of poles is desired, then there is a reduction in the core material available, for a fixed volume. Finally, for each pole pair that is introduced, there is an increase in the copper loss. The close coupling of pole number, copper and core area lead to strong restraints on geometrical optimizations.

Use of the transverse flux configuration leads to a decoupling of the space requirements for the core

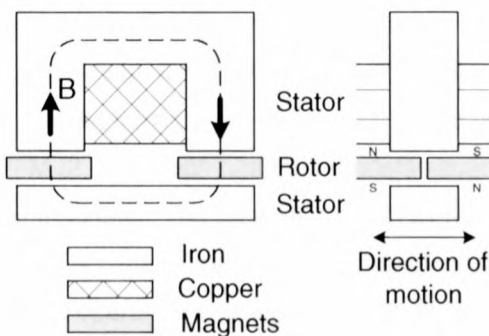


Figure 1.1: *Cross section of transverse flux machine*

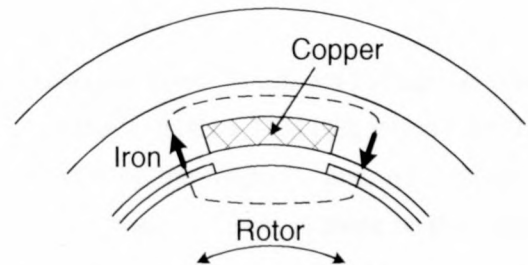


Figure 1.2: *Cross section of longitudinal flux machine*

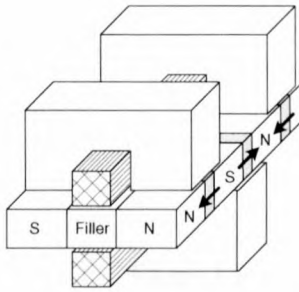


Figure 1.3: *Double sided TFM with flux concentration [1]*

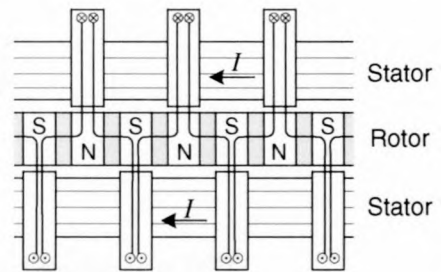


Figure 1.4: *Cross section of double sided TFM with flux concentration [1]*

material and the windings. With this configuration the number of poles can be increased indefinitely (at least until the pole pitch becomes vanishingly small), without affecting the current loading. The active face of the core can also be optimized without affecting the current loading. This high level of geometrical flexibility results in a much easier optimisation process.

In [1], Weh also suggested two other geometrical configurations. Initially, the machine can be double sided, which leads to a doubling of the force on the rotor. Another configuration has the magnets arranged in a flux concentrating configuration. Iron flux guides are placed between the magnets, which are magnetized tangential to the direction of force on the rotor. This configuration improves the utilization of the magnets [1]. Fig. 1.4 and Fig. 1.3 show the double sided TFM with flux concentration. This type of configuration, with the magnets situated on the rotor, is known as the active rotor TFM. Further variants of this type of TFM are presented in [2–10]. Notably, [10] presents very good construction concepts.

The transverse flux configuration results in machines with relatively high power (or torque) densities, i.e. the torque/power output to size/weight ratio is very good. A high power density machine can lead to many improvements in current machine applications. One of the main areas of interest is direct drives for traction applications. Removal of gear boxes in traction applications could reduce cost, weight and space requirements. Other than traction, direct drives could be used in wind generators, which usually make use of very high gear ratios. There may also be wide spread applications in military applications, where direct drives could be used for devices such as turret servos. TFMs are also currently being developed for naval applications [11], where space saving high torque machines are needed. Essentially, any electrical machine application that makes use of gears, or has stringent space requirements, can benefit from a machine with a high power/torque density.

Apart from the active rotor TFM, two other types of TFM can be defined. These are the passive rotor TFM [2, 12], which has the magnets situated on the stator, and the reluctance TFM [13], which contains no magnets. The passive rotor TFM relieves centrifugal stresses on the magnets, and, as a result of direct access to the magnets, makes cooling of the magnets much easier. Both of these factors make higher operational speeds possible. Husubek's reduced magnet material passive rotor TFM [12] presents one solution for this type of TFM. As can be seen from Fig. 1.5, this machine is essentially the same as Weh's double sided configuration, with the copper moved to the filler's position. The copper, magnets and flux concentrating parts now form the stator, with iron blocks forming the rotor. A factor of concern with

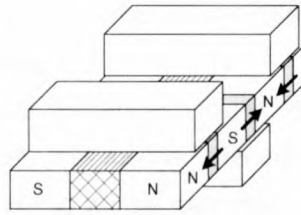


Figure 1.5: *Hasubek's reduced magnet material passive rotor TFM*

Hasubek's design is the effect of radial forces acting to attract the rotor toward the stator. If these forces are not properly balanced they could lead to significant operational problems. Another consideration is the complexity that a rotor plate with extrusions presents to the construction of the machine, especially if there are extrusions on both sides of the rotor plate.

The reluctance TFM is a TF version of the switched reluctance machine, and is only electrically excited. The reluctance TFM requires only unidirectional currents, which results in a simpler power converter, and reduced magnetic losses. Also, the absence of magnets reduces the cost of the machine. Simplicity and cost need to be weighed against reduced output and higher torque ripple, when compared to active and passive rotor TFMs.

By its nature the TFM has a 3-dimensional (3D) flux path. This eliminates laminated iron as a viable core material, as eddy current losses are high, and it is difficult to bend the laminations to form an accurate path for the flux. Soft magnetic composites (SMC) offer a solution to this problem [14]. SMC consists of pure iron particles with a resin surface coating which are pressed and then sintered to form a component. The composition of the material results in a low conductivity, leading to highly reduced eddy currents, and the possibility of higher operating frequencies. The isotropic nature of SMC means that a 3D flux path is now viable. SMC has been successfully used to reduce the size and improve the output and construction of some electrical machines [15], [16]. SMC does have disadvantages though, namely, its permeability is much lower than pure iron, and the hysteresis losses are higher. Total core losses, including eddy current losses, are still lower in SMC than in pure iron for higher operating frequencies. Even with its shortcomings, most modern TFMs make use of SMC [8, 10], at least in areas of three dimensional flux. [8] and [17] give special attention to the choice of material and the losses associated with different materials in active rotor TFMs.

1.2 Summary

This thesis presents the evaluation of various TFM configurations with the goal of constructing a 50 kW machine that could fit into the hub of a standard sedan wheel. Various configurations of the reluctance, active rotor and passive rotor TFM are evaluated using 3D-finite element analysis. Reluctance TFMs with and without magnetic shielding are evaluated simply by comparing the motoring and extraneous forces produced on the rotor. To evaluate and compare different active and passive TFM configurations the volume of the machine is kept constant and the pole dimensions optimised for maximum torque output.

One of the passive rotor configurations is decided upon, and this is followed by an in depth analysis of the simulation results for the particular topology.

The relevant machine parameters are derived, and this is followed by an investigation into the torque of multi-phase machines. Next the power loss mechanisms are examined and heat transfer simulations are done to determine what type of cooling will be necessary. To complete the design a control system is derived using the state-space method. Simulations of both current control and speed control are presented.

A passive rotor TFM was constructed based upon the simulation results. The construction process presented many difficulties, which resulted in the machine not operating as desired. The construction and problems are presented and discussed. Certain limitations could be overcome and the machine was tested in generator mode. These measurements are presented. Finally conclusions are drawn and recommendations made.

Chapter 2

Design and Optimisation

2.1 Introduction

In this chapter the magnetic design process is detailed. A 3D finite element (FE) package (Magnet 6.11.1, Infolytica Corp.) is used to analyse different topologies and weigh them against each other. Each topology is considered in terms of motoring torque, cogging torque, and extraneous forces acting on the rotor. By making use of appropriate boundary conditions it is possible to analyse only one pole pair of each topology and then factor the results by the number of pole pairs to obtain results for the entire phase. Due to the phases being electrically decoupled it is possible to obtain results from only a single phase and then use superposition to determine the effect of multiple phases (this is done in Chap. 3). TFMs normally have small pole pitches, and as a result it is possible to make use of linear instead of rotary models. To begin, different configurations of the reluctance TFM (RTFM) [13] are considered. Next, variations of the RTFM making use of permanent magnets (PMs) as flux guides/screens are examined. The following section aims to compare the different active and passive rotor configurations of the TFM. To do this an optimisation algorithm is devised and applied to different topologies. In this optimisation the volume and copper losses of the machine are kept constant. Finally a short summary of the different active and passive rotor configurations is presented and a particular topology chosen.

2.2 Reluctance TFMs

2.2.1 C-core RTFM

Fig. 2.1 shows a FE model for a single pole of a RTFM, which is based on Weh's RTFM [13]. The core material is Somalloy 500, an SMC product from Höganäs AB, Sweden. Magnetic data for the material was obtained from Höganäs AB and imported into the FE program (for data see Appendix A). The initial dimensions and the axis system used for the FE models is shown in Fig. 2.2. The X-direction is longitudinal, the Y-direction radial and the Z-direction axial to the direction of motion.

The initial component size was chosen fairly small for three main reasons,

1. One of the initial goals is to design a motor that fits into the hub of a sedan car's wheel

curves for this configuration. In this case, the cogging forces are reduced to zero, but the motoring force is approximately the same as for the simple C-Core RTFM. Also shown is the radial force acting on the rotor, which is not balanced in this case. The rotor block provides a low reluctance path for the magnets' field, which seems to be the source of the undesired effects of this configuration.

2.4 Active and Passive Rotor TFMs

As already discussed in Sec. 1.1, most of the research that has been done into TFMs has been focused on the active rotor (AR) configuration of the TFM. Significantly sized magnets are placed on the rotors of these TFMs. Another alternative has the magnets situated on the stator of the machine and is known as the passive rotor (PR) TFM. The main advantages of the PR approach are direct access to the magnets for cooling and removal of centrifugal forces acting on the magnets. Direct access for cooling means that higher efficiency cooling systems (such as liquid cooling) can be implemented more easily, and the removal of centrifugal forces on the magnets can lead to a potentially simpler construction. For AR and PR TFMs it is possible to produce constant motoring torque, except at fully aligned and unaligned positions. This makes it possible to make use of only two phases for a machine.

In this section FE analysis is used to determine the torque characteristics for different topologies of active and passive rotor TFMs. In preliminary FE simulations, with equal pole volume, it was seen that each topology is sensitive in a unique way to the relationship between the stator core size and the magnet size. This makes it difficult to compare topologies by keeping the magnet volume constant. It was decided that instead of following a constant magnet volume approach, that each topology would be analysed and optimised independently. The results of these analyses are tabulated and discussed at the end of this section. Based on the analysis and certain preliminary construction constraints one of the PR topologies is chosen for a detailed study.

2.4.1 Optimisation

To optimise the TFM designs a simple optimisation program was written making use of the FE package's scripting language (VBScript). Initially, the magnet volume as a percentage of the pole volume is determined manually. The magnet percentage, copper losses and pole volume are then kept constant, and the algorithm attempts to optimise the output torque by varying the inner dimensions of the FE model. This optimisation is only done for one position ($\theta_{elec} = -90^\circ$). In this position the cogging torque is zero. The algorithm is basically a line maximisation [19] technique that is applied to each dimension independently and maximises the function $T = f(x)$, where T is the torque and x is one of the dimensions. Torque is calculated for the initial dimensions, and then the inner dimensions are varied one at a time. One dimension is incremented by a fixed step until it is seen that the torque begins to decrease. If it is seen that the torque is lower than the initial torque on the first step, then the dimension is decremented until the torque begins to decrease. The maximum value calculated and the two points on either side of it are said to bracket the maximum value of the function. Once the three points closest to the peak have been determined a

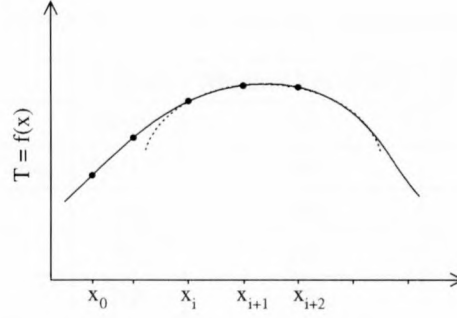


Figure 2.16: Interpolation of three points bracketing a maximum

second degree polynomial of the Newton form is fitted to these three values. This polynomial has the form

$$f(x) = c_1 + c_2(x - x_i) + c_3(x - x_i)(x - x_{i+1}), \quad (2.1)$$

where

$$\begin{aligned} c_1 &= f(x_i) \\ c_2 &= \frac{f(x_i) - f(x_{i+1})}{(x_i - x_{i+1})} \\ c_3 &= \frac{c_2}{x_i - x_{i+2}} - \frac{f(x_{i+1}) - f(x_{i+2})}{(x_{i+1} - x_{i+2})(x_i - x_{i+2})}. \end{aligned} \quad (2.2)$$

Fig. 2.16 is a graphical representation of this process, where the solid line is the function, $T = f(x)$, and the dotted line is the interpolation function. Eqn. (2.3) can be found by setting the derivative of Eqn. (2.1) to zero. Solving for x_{optim} then yields the dimension at which the maximum torque is achieved,

$$x_{optim} = \frac{1}{2} \left(x_{i+1} + x_i - \frac{c_2}{c_3} \right). \quad (2.3)$$

After one of the dimensions has been optimised, the next dimension is optimised and the process is iterated until the change in the dimensions is negligible.

For each step a new current value is determined by

$$I = \sqrt{\frac{P_{Cu_{loss}}}{R_{Cu}}}, \quad (2.4)$$

where

$$R_{Cu} = \frac{2\pi r_{mean} N}{\sigma A_{Cu} f}, \quad (2.5)$$

with r_{mean} the mean radius of the coil, N the number of windings, A_{Cu} the cross sectional area of the copper, f the fill factor and R_{Cu} the resistance of the coil. f is typically ≈ 0.5 and $P_{Cu_{loss}}$ was chosen as 66 W , as this value was calculated from the parameters of the reluctance TFM simulations. Table 2.1 details the symbols and dimensions that are common to all the topologies, which are also shown graphically in Fig. 2.18. The comments in Table 2.1 describe each dimension's role in the optimisation algorithm.

To determine the pole length the hub of a sedan car's wheel was measured, and it was seen that a machine with an outer diameter of 280 mm would comfortably fit into the hub. In preliminary simulations it

Table 2.8: Comparison of different active and passive rotor TFM's

Topology	\bar{T} [Nm]	Magnet Vol. [cm^3]	$\bar{T}/\text{Magnet Vol.}$ [$\frac{Nm}{cm^3}$]
U-Core AR	80/95	50	1.6/1.9
U-Core AR Flux Conc.	98/112	107	0.92/1.04
C-Core PR	116	245	0.47
RMM PR	55	69	0.8
I-Core PR	105	98	1.07
U-Core PR	89/106	214	0.42/0.5
		$\bar{T}/\text{Vol.}$ [$\frac{Nm}{cm^3}$]	$\bar{T}/\text{Active mass}$ [$\frac{Nm}{kg}$]
U-Core AR		0.032/0.038	20.4/24.2
U-Core AR Flux Conc.		0.042/0.045	16.5/18
C-Core PR		0.047	17.3
RMM PR		0.022	11
I-Core PR		0.043	17.4
U-Core PR		0.036/0.043	11.7/14.5

Table 2.9: Material densities

Material	Density ρ [g/cm^3]
Copper	8.9
NeFeB	7.5
Somalloy	7.32

shows the motoring and cogging torque curves for this topology.

2.5 Summary

Table 2.8 gives a comparison of some of the characteristics of the different AR and PR configurations of the TFM, and serves as the basis for choosing a suitable topology. The values given are for a single phase of a machine and in the cases where two values are given, the first is for an internal rotor, and the second for an external rotor. This data was obtained and calculated from the simulations, optimum dimensions, and the material densities given in Table 2.9. It should also be noted that the torque values can be raised by increasing the copper losses. There are some interesting things to note, namely,

1. The topology with the highest torque per magnet volume is the only topology which does not use flux concentration. It is possible that this could be a simulation fault, as flux concentrating topologies are supposed to make better use of the magnets. Another possibility is that this configuration results in less fringing flux, leading to higher output. This is also the topology with the highest torque to weight ratio.
2. The U-Core and C-Core topologies have the largest amount of magnet material, and thus the lowest torque to magnet volume ratio.

3. Overall the I-Core topology performs well in all the categories

Based on this data a preliminary investigation into the construction of an I-Core PRTFM was done. The following things were considered and the outcome of the investigation is given below each item.

1. The production of the SMC blocks

- (a) The cost of producing the SMC pieces through pressing and sintering was too high due to the tooling costs. For the I-Core topology three different tools would be needed (inner and outer stator, and rotor tooling).
- (b) Höganäs AB was prepared to provide a standard shape SMC cylinder which could then be machined to the correct dimensions.
- (c) Wire cutting was investigated as a machining technique due to the high accuracy with which the parts could be cut. Due to high cost this was also eliminated as an option.
- (d) Conventional machining techniques were attempted, but due to the brittle nature of SMC these techniques failed for the shape of the parts needed.

2. General mechanical construction issues that may be encountered

- (a) The biggest issue would be the difficulty in mounting the rotor blocks and assembling the rotor plate to the machine. This does not block the construction of this type of machine, but could cause many assembly issues.

3. Heat management for the machine

- (a) A preliminary heating simulation was done using the same method as Chap. 4. This helped to give an idea of what type of cooling system would be needed (e.g. heat sink with forced air cooling). The simulations showed no serious limiting factors

From this preliminary investigation it became clear that there was no financially viable means to manufacture the SMC components needed to construct the I-Core PRTFM. The U-Core PRTFM was then examined mainly with the manufacturing of the SMC components in mind. With this topology there are effectively only two different SMC components that need to be manufactured. It was also found that it was possible to machine the necessary components using conventional machining techniques. The assembly of this topology is also easier due to the ability to slide the rotor into the stator, as with a conventional machine. Further, an internal rotor machine was decided upon, due to the potential for easier assembly.

With these factors in mind it was decided to construct a machine based upon the U-Core PRTFM topology. The rest of this thesis focuses on the analysis, construction and measured results of a U-Core PRTFM.

Chapter 3

Analysis of Simulation Results

3.1 Introduction

This chapter presents further analysis of the results obtained from the simulations. The flux linkage data is used to obtain the inductance and back EMF of the U-Core PRTFM. The inductance varies with position, and the Park transform is used in an attempt to obtain an inductance that does not vary with position. The motoring and cogging torque for multi-phase machines is calculated, and the effect on torque ripple is examined.

3.2 Machine Parameters

The U-Core PRTFM has magnetically decoupled phases, and thus, the voltage at the terminals of one phase of the machine is,

$$v_a = i_a r_a + \frac{d\lambda_a}{dt}, \quad (3.1)$$

where v_a , i_a , r_a and λ_a are, respectively, the voltage, current, resistance and flux linkage of the phase. For this machine the flux linkage is a function of the current and the position of the rotor,

$$\lambda_a = F(i_a, \theta). \quad (3.2)$$

Because both i_a and θ are functions of time, the voltage equation can be written,

$$v_a = i_a r_a + \left(\frac{\delta \lambda_a}{\delta i_a} \right) \frac{di_a}{dt} + \left(\frac{\delta \lambda_a}{\delta \theta} \right) \omega_e. \quad (3.3)$$

With the inductance $L_a = \left(\frac{\delta \lambda_a}{\delta i_a} \right)$ and the back-emf $e_a = \left(\frac{\delta \lambda_a}{\delta \theta} \right) \omega_e$, Eqn. (3.3) can be rewritten as,

$$v_a = i_a r_a + L_a \frac{di_a}{dt} + e_a. \quad (3.4)$$

Eqn. (3.4) can be represented by a simple electrical model which is shown in Fig. 3.1.

where l_w is the length of the wire, σ is the conductivity, and A_w is the cross-sectional area of the wire. If the machine is operated at speeds up to 1500 rpm, then the frequency can be up to 1250 Hz. This is much higher than conventional machines which means the skin effect should also be taken into account. The skin depth is given by,

$$\delta = \sqrt{\frac{2}{\omega\mu\sigma}}, \quad (3.16)$$

where ω is the frequency in $rad.s^{-1}$ and μ is the permeability. The conductivity of copper is $\sigma = 5.65 \times 10^7$ and the permeability is $\mu = 4\pi \times 10^{-7}$, which yields a skin depth of

$$\delta = 1.8692 \text{ mm @ } 1250 \text{ Hz}, \quad (3.17)$$

With a rated current of 40 A and a current density of 10 A/mm^2 , the cross sectional area of the copper wire should be 4 mm^2 . This results in a conductor diameter of 2.26 mm if conductors with a round cross section are used. The desired diameter is larger than the skin depth, which means that multiple conductors should be used. If two conductors are used in parallel, then 1.6 mm diameter conductors can be used, which is less than the skin depth.

Eqn. (3.15) can be written

$$r_a = \frac{2\pi r_{mean} N}{\sigma A_{Cu}}, \quad (3.18)$$

where r_{mean} is the mean radius of the copper, N the number of windings and A_{Cu} is the area of the copper wire (not the cross-sectional area of the copper). For the U-Core PRTFM $r_{Cu_{mean}} = 121.75 \text{ mm}$, $N = 34$, $\sigma = 5.65 \times 10^7$, and $A_{Cu} = 2 \times \pi(0.8 \times 10^{-3})^2$, which yields a resistance of

$$r_a = 114.48 \text{ m}\Omega. \quad (3.19)$$

3.2.5 Torque Approximation

The torque function for a single phase can be approximated by making use of Fourier series. This is done to aid in the design of the control system. The average torque per ampere can be determined by firstly finding the average torque for a specified current and then dividing the average by the current. This is done for each simulated current and an average of the results can then be taken to determine the average torque per ampere (see Appendix C, Sec. C.3),

$$K_T \approx 3.5 \text{ Nm.A}^{-1}. \quad (3.20)$$

The torque function has the form

$$\begin{aligned} T_m &= F(i_a, \theta) \\ &\approx K_T i (a_0 + a_1 \sin\theta + a_2 \sin^2\theta + a_3 \sin^3\theta + a_4 \sin^4\theta), \end{aligned} \quad (3.21)$$

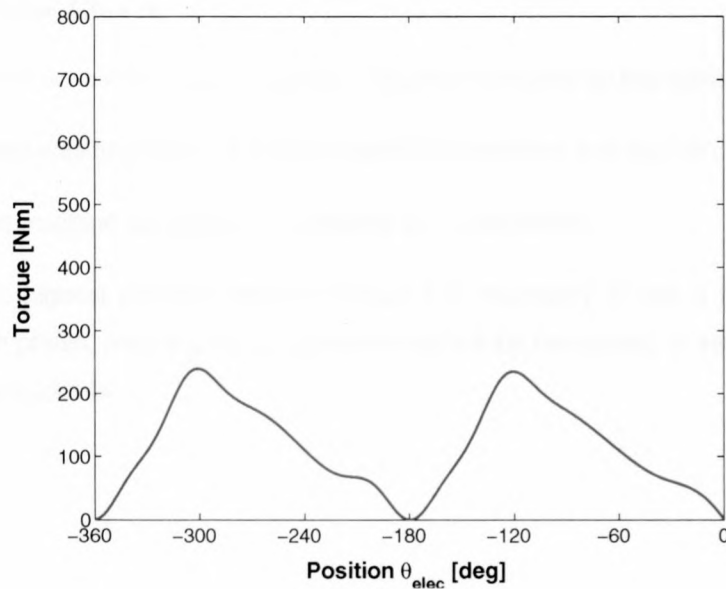


Figure 3.15: Single phase motoring torque of U-core PRTFM (40 A phase current)

3.3.2 Motoring Torque

Using the same method as the cogging torque the effects of multiple phases on the total average motoring torque can be determined. The highest average torque can be achieved by driving the machine with a DC current, which switches polarity every 180°_{elec} , i.e. the ideal current waveform is a square wave. The machine's current rating is 40 A and Fig. 3.15 shows the rated torque of a single phase. Figs. 3.16, 3.17 and 3.18 show the rated motoring torque for two, three and five phase machines respectively.

Fig. 3.19 shows the motoring torque ripple of multiphase machines normalised against the torque ripple of a single phase. As with the cogging torque the motoring torque ripple for machines with an uneven number of evenly spaced phases converges to zero sooner than machines with an even number of phases. Again, machines with an even number of phases and a phase offset of $\frac{180^\circ_{elec}}{N_p}$ diverge after a certain point.

Even though both cogging torque- and motoring torque-ripple benefit when making use of a high number of phases, the cost may outweigh the benefits. There is not only the cost of the machine, but also the power converter to take into account. On the other hand, the magnetic circuit is made up of many small pieces, and the economics of scale may bring the cost of each phase down for full production models. A high number of duplicate components is also well suited to the SMC manufacturing process.

3.3.3 Final Machine Choice

It was decided to construct a three phase machine. The main reasons for this were,

1. The original idea was to construct a three phase 50kW machine and this can be achieved.
2. The cost of the machine will rise if more phases are constructed.
3. To achieve the highest possibly motoring torque it is necessary to use a full-bridge power converter for each phase, meaning that six phase-arms will be necessary. A seven phase-arm power converter was available.

Chapter 4

Heat Management

4.1 Introduction

All electrical machines have some form of loss mechanisms, which can result in heat, sound or vibration. The generation of heat forms a large part of the output of the loss mechanisms, and it is essential to control the heating of the motor. Permanent magnet machines are especially sensitive to heating, as the magnets have a limited temperature operating range. Overheating can lead to reduced performance and even failure of the machine. This chapter examines some of the loss mechanisms of the PRTFM and simulations are done to predict the necessary cooling techniques.

4.2 Loss Mechanisms

The main mechanisms involved in heating are,

1. Copper losses ($P = I^2R$),
2. Magnetic losses (hysteresis), and
3. Eddy current losses.

The TFM uses a simple coil winding, which results in very low total winding resistance. Thanks to this the copper losses in TFMs are, in general, very low. On the other hand, the magnetic losses are a material property, and SMC has high hysteresis losses. Hysteresis losses are frequency dependent, and thus are low at low frequencies, but increase with frequency. Eddy current losses are dependent on the frequency and the area that the magnetic field is passing through. Due to the nature of SMC the eddy current losses are very low. At high frequencies (> 100 Hz) the combination of core losses (hysteresis and eddy current) are typically lower when using SMC versus standard iron cores [14].

The hysteresis losses were determined from data obtained from Högånäs AB. The curve of loss vs. frequency is dependent on the process and mix of compounds used to manufacture the SMC. A data sheet for Somalloy 550 is given in Appendix A. For the purposes of the simulations the eddy current losses were assumed to be zero, but this may not be true in the high frequency operating range of the designed machine (frequencies up to 1250 Hz).

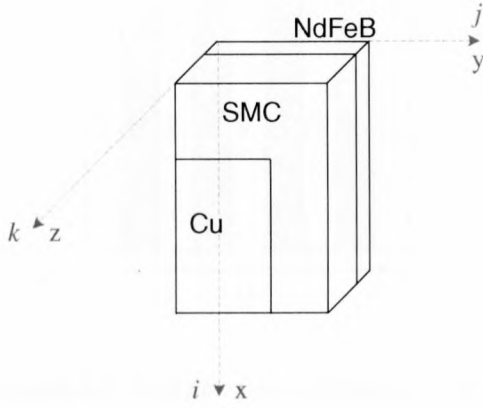


Figure 4.1: Stator Model for Thermodynamic Analysis

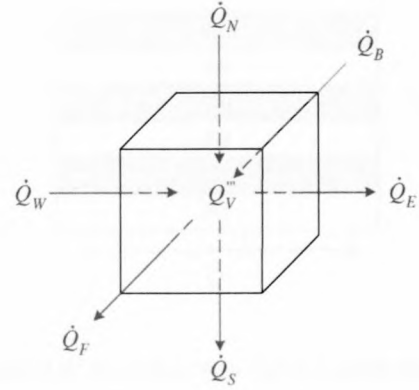


Figure 4.2: Control Volume

There are also other loss mechanisms, such as eddy current losses in the casing (due to fields outside of the active magnetic circuit), and eddy currents in the magnets (the magnets are good conductors), which are not taken into account. These losses are investigated in detail in [21].

4.3 Simulations

The machine's structure can be represented linearly, and then broken up into control volumes to analyze the temperature distribution in the machine. The model used for the thermodynamic analysis was a $\frac{1}{4}$ of a linearised pole, as shown in Fig. 4.1. It is possible to only use a $\frac{1}{4}$ of a pole due to symmetry of the heat flow. There are l control volumes in the x direction, m in the y direction and n in the z direction. Fig. 4.2 shows a control volume with heat flows \dot{Q}_N , \dot{Q}_S , \dot{Q}_W , \dot{Q}_E , \dot{Q}_B and \dot{Q}_F through its surfaces. \dot{Q}_V''' is heat generated within the control volume due to power losses in the machine.

The fundamental equation for each control volume is

$$\frac{\Delta E}{\Delta t} = \Sigma \dot{Q}_{in} - \Sigma \dot{Q}_{out}, \quad (4.1)$$

where E is energy and t is time. Eqn. (4.1) can also be expressed in terms of the change in temperature as

$$MC \frac{\Delta T}{\Delta t} = \Sigma \dot{Q} \quad (4.2)$$

where M is the mass, C is the specific heat capacity, T is the temperature and $\Sigma \dot{Q} = \Sigma \dot{Q}_{in} - \Sigma \dot{Q}_{out}$. It follows that

$$T^{t+\Delta t} = T + \frac{\Sigma \dot{Q}}{MC} \Delta t \quad (4.3)$$

where

$$\Sigma \dot{Q} = \dot{Q}_N - \dot{Q}_S + \dot{Q}_W - \dot{Q}_E + \dot{Q}_B - \dot{Q}_F + \dot{Q}_V''' \quad (4.4)$$

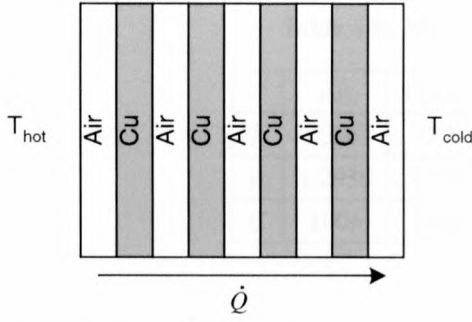


Figure 4.3: Heat flow perpendicular to copper strands

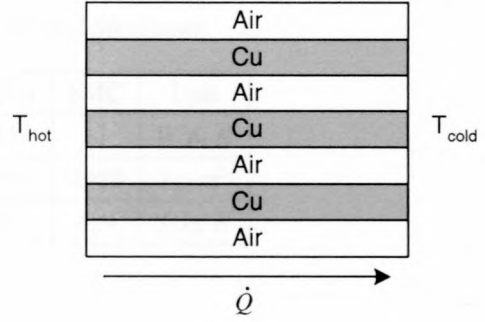


Figure 4.4: Heat flow parallel to copper strands

For heat transfer by convection the following hold

$$\dot{Q}_{N_{i,j,k}} = \frac{-kA_N(T_{i,j,k} - T_{i-1,j,k})}{\Delta x} \quad (4.5a)$$

$$\dot{Q}_{S_{i,j,k}} = \frac{-kA_S(T_{i+1,j,k} - T_{i,j,k})}{\Delta x} \quad (4.5b)$$

$$\dot{Q}_{W_{i,j,k}} = \frac{-kA_W(T_{i,j,k} - T_{i,j-1,k})}{\Delta y} \quad (4.5c)$$

$$\dot{Q}_{E_{i,j,k}} = \frac{-kA_E(T_{i,j+1,k} - T_{i,j,k})}{\Delta y} \quad (4.5d)$$

$$\dot{Q}_{B_{i,j,k}} = \frac{-kA_B(T_{i,j,k+1} - T_{i,j,k})}{\Delta z} \quad (4.5e)$$

$$\dot{Q}_{F_{i,j,k}} = \frac{-kA_F(T_{i,j,k} - T_{i,j,k-1})}{\Delta z}, \quad (4.5f)$$

where k is thermal conductivity of the material and A is the surface area of the control volume. On the surfaces $j = 0$, $k = 0$ and $k = n$ there is no heat flow due to the symmetry of the machine. All the other external surfaces transfer heat according to Eqn. (4.6),

$$\dot{Q}_{i,j,k} = hA(T_e - T_{i,j,k}), \quad (4.6)$$

where h is the heat transfer coefficient and T_e is the environmental temperature.

Due to the copper not being one solid piece, but a bundle of strands, the thermal conductivity varies with the direction of heat flow. There is good conductivity along the length of the copper, but from strand to strand the conductivity is much lower. Fig. 4.3 and Fig. 4.4 illustrate this. For heat flow in the copper in the x and y directions Fig. 4.3 applies and

$$k_{\perp} = \frac{k_{Cu}k_{Air}}{\alpha k_{Cu} + (1 - \alpha)k_{Air}}, \quad (4.7)$$

where α is the void factor (1 - fill factor), which is typically $\alpha = 0.5$. For heat flow in the copper in the z direction, Fig. 4.4 applies and

$$k_{\parallel} = \alpha k_{Air} + (1 - \alpha)k_{Cu}. \quad (4.8)$$

Another area that the thermal conductivity varies is on the surfaces where two different materials

Table 4.1: Material Properties for Thermal Simulation

	Air	Epoxy	Copper	Magnet	SMC	Unit
k	0.0267	0.2	401	8.95	17	$W/m K$
ρ	1.2930	1250	8900	7500	7320	kg/m^3
C	1006	1400	385	460	419	$J/kg K$

touch each other. With the thermal resistance

$$R_T = \frac{\Delta x}{kA}, \quad (4.9)$$

the heat transfer through the surface can be written as

$$\begin{aligned} \dot{Q} &= \frac{T_{hot} - T_{cold}}{\Sigma R_T} \\ &= \frac{T_{hot} - T_{cold}}{\frac{\Delta x_1}{2k_1A} + \frac{\Delta x_2}{2k_2A}} \end{aligned} \quad (4.10)$$

The material properties used in the simulations are shown in Table 4.1

Using Eqn. (3.19) (pp. 33) the copper losses at rated current (40 A) are $P_{Cu_{loss}} = 183 W$. Only a $\frac{1}{4}$ of a pole is used in the simulation, which means that the total copper loss should be divided by 400 to find the copper loss for the simulated volume. In the simulation the dissipated power is evenly distributed among all the copper elements. The magnetic losses depend on the speed of the motor, and from the SMC data sheets are as follows

$$P_{SMC_{loss}} = \begin{cases} 32 W/kg & @ 120 \text{ rpm (100 Hz)} \\ 200 W/kg & @ 600 \text{ rpm (500 Hz)} \\ 400 W/kg & @ 1200 \text{ rpm (1000 Hz)} \end{cases} \quad (4.11)$$

An arbitrary value of $h = 5$ was chosen for an initial simulation.

Preliminary simulations showed that the motor will overheat if running above 100 rpm. It was therefore decided to investigate the use of heat sinks, attached to the outside of the machine, with air flowing axially over them. The air flow could be generated either by an external fan, or by a fan that forms part of the rotor disc. It is possible to calculate a new equivalent heat transfer coefficient to bring the effect of the heat sink into the simulation. To determine the new h value, the heat transfer coefficient of the air flowing through the heat sink and the efficiency of the fins must be calculated.

Fig. 4.5 shows the fins and dimensions of the heat sink. The air flows through the area between the fins. An equivalent diameter for this area can be found

$$D_h = \frac{4A}{P}, \quad (4.12)$$

where,

$$A = bL \text{ and } P = 2(b + L). \quad (4.13)$$

The Renold's number can then be found by

$$Re_h = \frac{\rho v D_h}{\mu_e}, \quad (4.14)$$

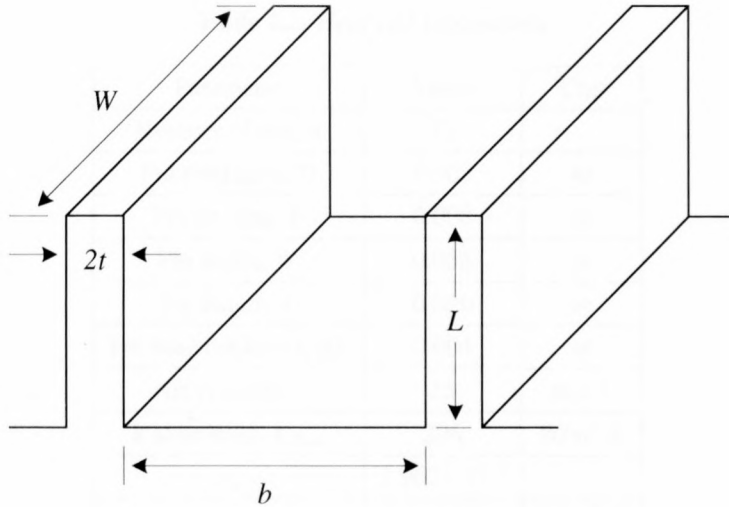


Figure 4.5: Heat sink fins

and

$$h_c = \frac{k}{D_h} Nu_h \left[W/m^2 K \right]. \quad (4.15)$$

Nu_h is the Nusselt number and is given by

$$Nu_h = \begin{cases} 0.023 Re_h^{0.8} Pr^{0.4} & \text{where } Re_h > 10000 \\ \frac{(f/8)(Re_h - 1000)Pr}{1 + 12.7(f/8)^{1/2}(Pr^{2/3} - 1)} & \text{where } 3000 < Re_h < 10^6 \end{cases}, \quad (4.16)$$

where

$$Pr = \frac{\mu_e C}{k} \quad (4.17)$$

$$f = (0.790 \ln Re_h - 1.64)^{-2}. \quad (4.18)$$

The efficiency of each fin can be determined by

$$\eta_f = \frac{\tanh \chi}{\chi}, \quad (4.19)$$

where

$$\chi = \beta L \quad \text{with} \quad \beta = \sqrt{\frac{h_c P}{k A_{CS}}}. \quad (4.20)$$

P is the perimeter around one of the fins, i.e. $P = 2(2t + W)$, k is the thermal conductivity of the fin material, and A_{CS} is the cross sectional area of one fin, i.e. $A_{CS} = 2tW$. The overall efficiency of the heat sink can be determined by

$$\eta_t = 1 - \frac{A_f}{A_f + A_b} (1 - \eta_f). \quad (4.21)$$

A_f is the total surface area of the fins, $A_f = 2nWL$, and A_b is the total surface area of the base, $A_b = nbW$, with n the total number of fins.

Table 4.2: Heat sink parameters

Parameter	Value	Unit
Number of fins, n	72	
Fin thickness, $2t$	0.005	m
Fin spacing, b	0.008	m
Fin width, W	0.056	m
Fin length, L	0.020	m
Fin base thickness, Δb	0.004	m
Air velocity, v	25	$m.s^{-1}$
k aluminum, k_{alum}	206	$W/m^2 K$
μ_e	1.962×10^{-5}	
u_c	401	$W/m^2 K$

A new heat transfer coefficient which takes the effect of the heat sinks into account can be calculated by

$$u_c = \frac{1}{A_{bb} \left(\frac{1}{h_c \eta_f (A_f + A_b)} + \frac{\Delta b}{k A_{bb}} \right)} \left[W/m^2 K \right] \quad (4.22)$$

where A_{bb} is the total area of the heat sink in contact with the motor, and k is the thermal conductivity of the heat sink material. The first term under the line represents the fins, and the second term represents the thermal resistance through the base of the heat sink.

Table 4.2 shows the parameters for the heat sink. The final heat transfer coefficient, u_c , was determined empirically by running simulations at full power until it was seen that the final temperatures fell within a reasonable range. To achieve this heat transfer it is necessary to have a relatively high air velocity. The heat transfer coefficient could also be achieved by making use of water cooling.

Simulations were done using this new coefficient to determine the heat distribution in the machine. Fig. 4.6 shows the temperature for one control volume on the side of the machine for three different cases of rotational speed. It is interesting to note that the rate of increase of the temperature is quite high.

Chapter 5

Construction

5.1 Introduction

The TFM presents significant construction challenges. Conventional machines usually rely on punched or laser cut laminations, whereas the TFM is made up of many small SMC and magnetic components. One of the main challenges is determining a method to connect all the pieces. The TFMs construction does have advantages though, namely, if the phases are constructed as individual units, it should be relatively easy to remove and replace a faulty phase. The winding structure is also very simple. This chapter details the process that was used to manufacture the components, and assemble the U-Core PRTFM.

5.2 Construction Process

5.2.1 Mechanical Design and Component Manufacturing

Some basic construction decisions were made in the beginning of the construction phase, which helped to form the outline and assembly for the machine. They were,

- The stator or each phase would be constructed individually, and then assembled to form a whole
- The rotor would be a single unit
- The basic components of the machine are,
 1. Stator SMC block
 2. Rotor SMC block
 3. Stator magnet
 4. Copper winding
- High temperature epoxy would be used to cast the stator components together to form a single phase
- Conventional machining techniques needed to be used due to financial constraints

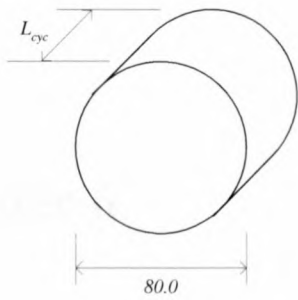


Figure 5.1: SMC cylinders used to machine components

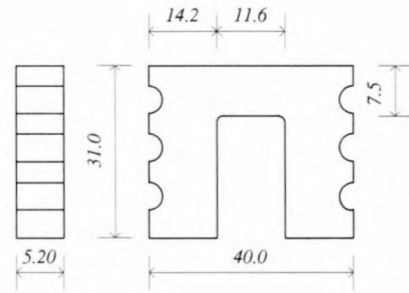


Figure 5.2: Stator SMC block outline and dimensions

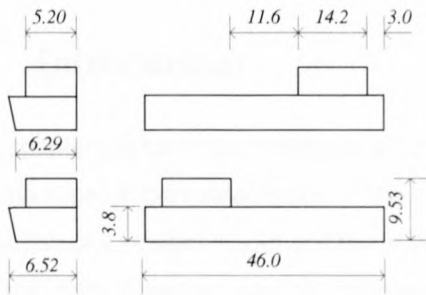


Figure 5.3: Rotor SMC block outline and dimensions

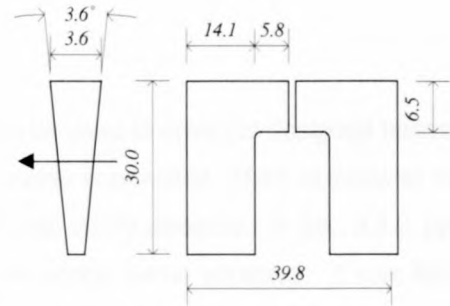


Figure 5.4: Stator magnet outline and dimensions

It was first necessary to generate engineering drawings of the machine. The final complete set of drawings is given in Appendix B. For more clarity simplified drawings are provided in the text. Once the drawings had been generated a method for machining the SMC pieces needed to be determined.

Pressed SMC cylinders were received from Högånäs AB, which were dimensioned for the I-Core TFM, as the I-Core had shown good simulation performance. As a result of not being able to machine the necessary I-Core TFM components, it was then necessary to determine a method to machine the U-Core components from the SMC cylinders available. The SMC cylinders had dimensions as shown in Fig. 5.1, with $L_{cyc} = 42\text{ mm}$ or 23 mm . It was found that these SMC cylinders could be cut into slices (along the length), ground to the correct thickness, and then machined to the correct shape with a CNC milling machine.

The stator SMC block outline and dimensions are given in Fig. 5.2. It can be seen that there are cut-outs in the side walls of the block. These cut-outs were added to allow the epoxy to flow into these gaps and secure the blocks to the frame. Two of these blocks were cut from each SMC slice.

The rotor SMC block outline and dimensions are given in Fig. 5.3. There are two blocks which together form one pole pair. Six blocks were machined from a slice of SMC. The slanted face was then machined on a normal milling machine. It can be seen that a small lip was added on both sides of the rotor block. The lip fits underneath a retaining ring which is one of the means employed to ensure that the blocks do not detach from the rotor.

Chapter 6

Control

6.1 Introduction

This chapter presents the design of a control system which can be used to drive the designed transverse flux machine. A brief description of the control system components is provided, which is followed by the derivation of a system model and the state-space equations. It was briefly discussed in Sec. 3.2.3, pp. 31, that the control system can be designed using the rotating reference frame variables. It was decided to design using the three-phase variables to save on the digital signal processor's (DSP) computation effort. To simplify the design of the control system the torque is approximated as a constant, which means that a constant current results in a constant motoring torque (rather than following the curve described in Eqn.(3.21)). The design of the controller is further simplified by adding a decoupling voltage to remove the effects of the back EMF. Both current control and speed control schemes are presented. The speed control is done for a three phase machine. From the simulation results it is seen that it is necessary to compensate for the load torque when controlling the speed, which is done by effectively designing an integral controller. Once the design is completed the more complex variation of parameters is taken into account, such as varying inductance and a more accurate torque function. This is followed by an investigation into the DSP effects, such as sampling rates and measurement resolution.

6.2 System Overview

Fig. 6.1 shows an overview of the control system. The machine consists of three phases which are offset by 120°_{elec} and are linked mechanically by the rotor. A full-bridge three phase power converter provides independent currents for each phase. This means that all three phases can be driven at the same time to provide the maximum possible torque output (i.e. square wave current inputs). A DSP controller provides the input to the power converter and samples the three phase currents. A resolver provides the position feedback which is also converted to a feedback for the machine speed.

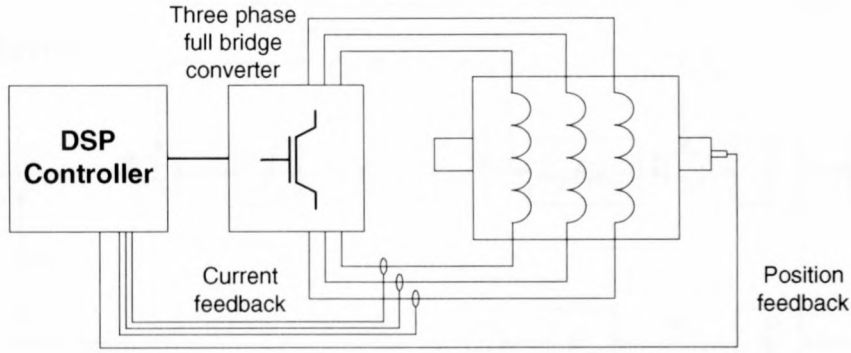


Figure 6.1: Control system overview

6.3 State-space Description

From the simulations it is seen that for a constant current the flux linkage of a single phase has the form,

$$\lambda_a = K_e \left[\cos \theta + a_1 \cos^2 \theta + a_2 \cos^3 \theta + \dots \right] + K_{e_{dc}}, \quad (6.1)$$

and if the flux linkage is approximated by the flux linkage at 0A, then,

$$\begin{aligned} \lambda_a &\approx K_e \cos(\theta) \\ \Rightarrow \frac{\delta \lambda_a}{\delta \theta} \frac{d\theta}{dt} &\approx -K_e \sin(\theta) \omega_e \end{aligned} \quad (6.2)$$

The torque per phase of the machine is

$$\begin{aligned} T_m &= F(i_a, \theta) \\ &\approx K_T \cdot i_a \cdot F_T(\theta), \end{aligned} \quad (6.3)$$

where K_T is the average torque per ampere and $F_T(\theta)$ is given in Eqn. (3.21) (see Sec. 3.2.5, pp. 33). Further, the mechanics of the machine are

$$T_m - T_L = J \frac{d\omega_m}{dt} + B\omega_m, \quad (6.4)$$

where T_L is the load torque, J is the inertia, and B is the damping factor. If the damping is assumed to be zero, i.e. $B = 0$, then,

$$T_m - T_L = J \frac{d\omega_m}{dt}. \quad (6.5)$$

The relationship between the mechanical speed, ω_m , and the electrical speed, ω_e , is given by,

$$\omega_e = \frac{P}{2} \omega_m, \quad (6.6)$$

where P is the number of poles.

A system diagram of one phase of the machine can now be drawn making use of Eqns. 3.4 and 6.2 - 6.6, and is shown in Fig. 6.2. The general form of the state-space equations is,

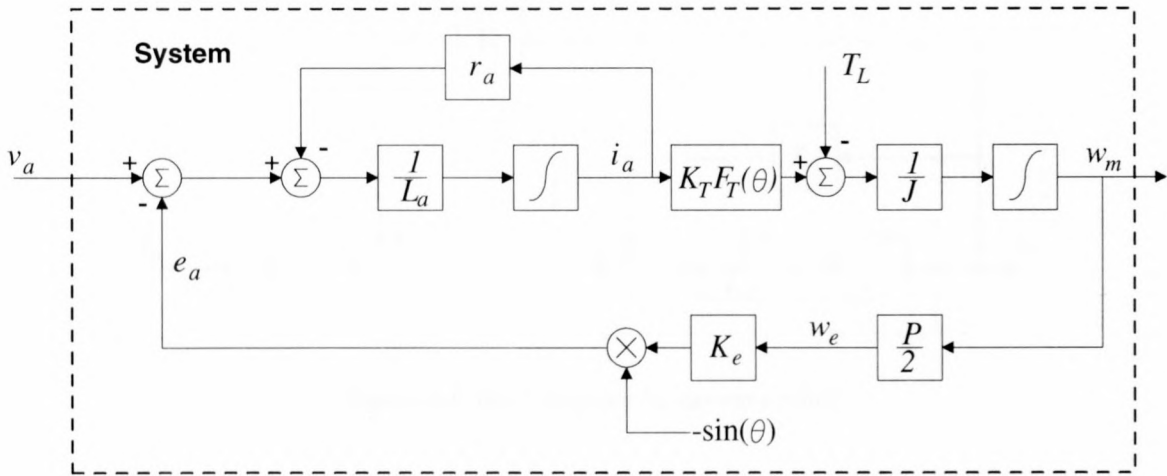


Figure 6.2: System diagram of a single phase machine

$$\begin{aligned} \dot{\mathbf{x}} &= \mathbf{F}\mathbf{x} + \mathbf{G}u, \\ y &= \mathbf{H}\mathbf{x} + \mathbf{J}u, \end{aligned} \tag{6.7}$$

with \mathbf{x} a matrix of the state variables, y the output, and u the control signal. If we define the state variables and control signal as,

$$x_1 = i_a \tag{6.8a}$$

$$x_2 = \omega_m \tag{6.8b}$$

$$u = v_a, \tag{6.8c}$$

the following can be derived from the system diagram,

$$\dot{x}_1 = \frac{1}{L'_a} \left(u - r_a x_1 + \frac{P}{2} K_e \sin(\theta) x_2 \right) \tag{6.9a}$$

$$\dot{x}_2 = \frac{1}{J} (K_T \cdot F_T(\theta) |x_1| - T_L) \tag{6.9b}$$

$$y = x_1. \tag{6.9c}$$

This results in the following state-space matrices,

$$\begin{aligned} \mathbf{F} &= \begin{bmatrix} -\frac{r_a}{L'_a} & \frac{PK_e \sin(\theta)}{2L'_a} \\ \frac{K_T \cdot F_T(\theta)}{J} & 0 \end{bmatrix} & \mathbf{G} &= \begin{bmatrix} 1 \\ 0 \end{bmatrix} \\ \mathbf{H} &= \begin{bmatrix} 1 & 0 \end{bmatrix} & \mathbf{J} &= 0 \end{aligned} \tag{6.10}$$

6.4 Current Control

6.4.1 Design

This section details the design of a current controller for a single phase of the machine. The control loop can be simplified by adding a decoupling voltage which leads to a much simpler system as shown in the

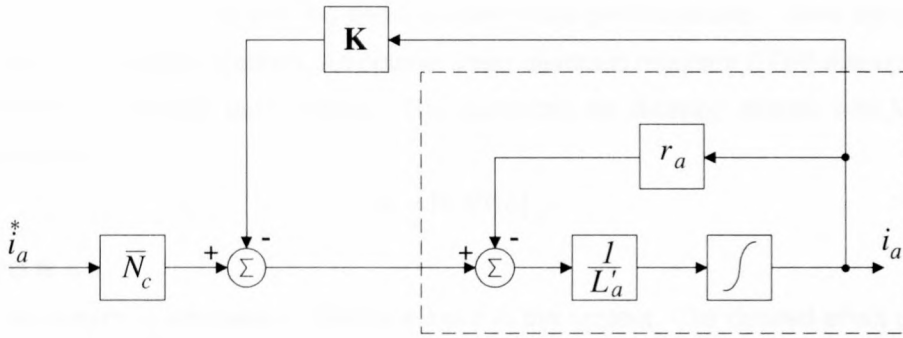


Figure 6.3: Block diagram for current control

block diagram Fig. 6.3. The decoupling voltage is an approximated back EMF which is then added to the system input signal. For design purposes it is assumed that this can be perfectly approximated and therefore the back EMF is canceled out. For the purposes of design the inductance is approximated as an average which can be determined from Fig. 3.5 (Sec. 3.2.3, pp. 30) as,

$$L'_a \approx 5 \text{ mH} \quad (6.11)$$

The following state equations can be derived from Fig. 6.3,

$$\dot{x}_1 = \frac{1}{L'_a} (u - r_a x_1) \quad (6.12a)$$

$$y = x_1. \quad (6.12b)$$

From Eqn. (6.12) the state-space matrices are

$$\begin{aligned} \mathbf{F} &= \begin{bmatrix} -\frac{r_a}{L'_a} \\ 0 \end{bmatrix} & \mathbf{G} &= \begin{bmatrix} \frac{1}{L'_a} \\ 0 \end{bmatrix} \\ \mathbf{H} &= [1] & J &= 0 \end{aligned} \quad (6.13)$$

Now that the state space matrices have been obtained, it is necessary to first determine where the closed loop poles of the system should be, and then to introduce a reference input for the system. The generalized control law of a state space system is given by Eqn. (6.14) [22],

$$u = -\mathbf{K}\mathbf{x} = - \begin{bmatrix} K_1 & K_2 & \dots & K_n \end{bmatrix} \begin{bmatrix} x_1 \\ x_2 \\ \vdots \\ x_n \end{bmatrix}. \quad (6.14)$$

Substituting Eqn. (6.14) into Eqn. (6.7) then yields,

$$\dot{\mathbf{x}} = \mathbf{F}\mathbf{x} - \mathbf{G}\mathbf{K}\mathbf{x}. \quad (6.15)$$

The characteristic equation of this closed-loop system is

$$\det [s\mathbf{I} - (\mathbf{F} - \mathbf{G}\mathbf{K})] = 0. \quad (6.16)$$

The gains \mathbf{K} are then chosen to give the desired closed loop pole locations. There are many ways of choosing the closed loop pole locations. An optimal linear quadratic regulator (LQR) attempts to minimize the control effort for a desired performance. The gains can be obtained directly with MATLAB's `lqr` function, which yields,

$$\mathbf{K} = [0.8916], \quad (6.17)$$

with $\mathbf{Q} = 1$ and $\mathbf{R} = 1$.

It is now necessary to introduce a reference input to the system. The desired effect is a zero error steady-state output, which means that the control law becomes,

$$u = u_{ss} - \mathbf{K}(\mathbf{x} - \mathbf{x}_{ss}), \quad (6.18)$$

so that when $\mathbf{x} = \mathbf{x}_{ss}$, i.e. no error, then $u = u_{ss}$. In the steady-state Eqn. (6.7) reduces to

$$\begin{aligned} \mathbf{0} &= \mathbf{F}\mathbf{x}_{ss} + \mathbf{G}u_{ss}, \\ y_{ss} &= \mathbf{H}\mathbf{x}_{ss} + Ju_{ss}. \end{aligned} \quad (6.19)$$

It is desired that $y_{ss} = r_{ss}$ for any value of r_{ss} . To achieve this we make $x_{ss} = \mathbf{N}_x r_{ss}$ and $u_{ss} = N_u r_{ss}$. Substituting this into Eqn. (6.19), the common factor r_{ss} cancels out to give the equation for the gains,

$$\begin{bmatrix} \mathbf{F} & \mathbf{G} \\ \mathbf{H} & J \end{bmatrix} \begin{bmatrix} \mathbf{N}_x \\ N_u \end{bmatrix} = \begin{bmatrix} \mathbf{0} \\ 1 \end{bmatrix}. \quad (6.20)$$

From this \mathbf{N}_x and N_u can easily be solved, and then used as a basis for introducing the reference input so as to get zero steady-state error to a step input,

$$\begin{aligned} u &= N_u r - \mathbf{K}(\mathbf{x} - \mathbf{N}_x r) \\ &= -\mathbf{K}\mathbf{x} + (N_u + \mathbf{K}\mathbf{N}_x)r. \end{aligned} \quad (6.21)$$

The coefficient of r in parenthesis is a constant that can be computed beforehand, and is given the symbol \overline{N} so that

$$u = -\mathbf{K}\mathbf{x} + \overline{N}r. \quad (6.22)$$

\overline{N}_c can now be calculated as,

$$\overline{N}_c = 1.0066. \quad (6.23)$$

6.4.2 Simulation

Fig. 6.4 shows the step response of the open- and closed-loop systems for current control. Two methods were used to generate these curves. Firstly, MATLAB's state-space and feedback functions were used, and a C program was written to simulate the system. It can be seen from Fig. 6.4 that the results are nearly identical.

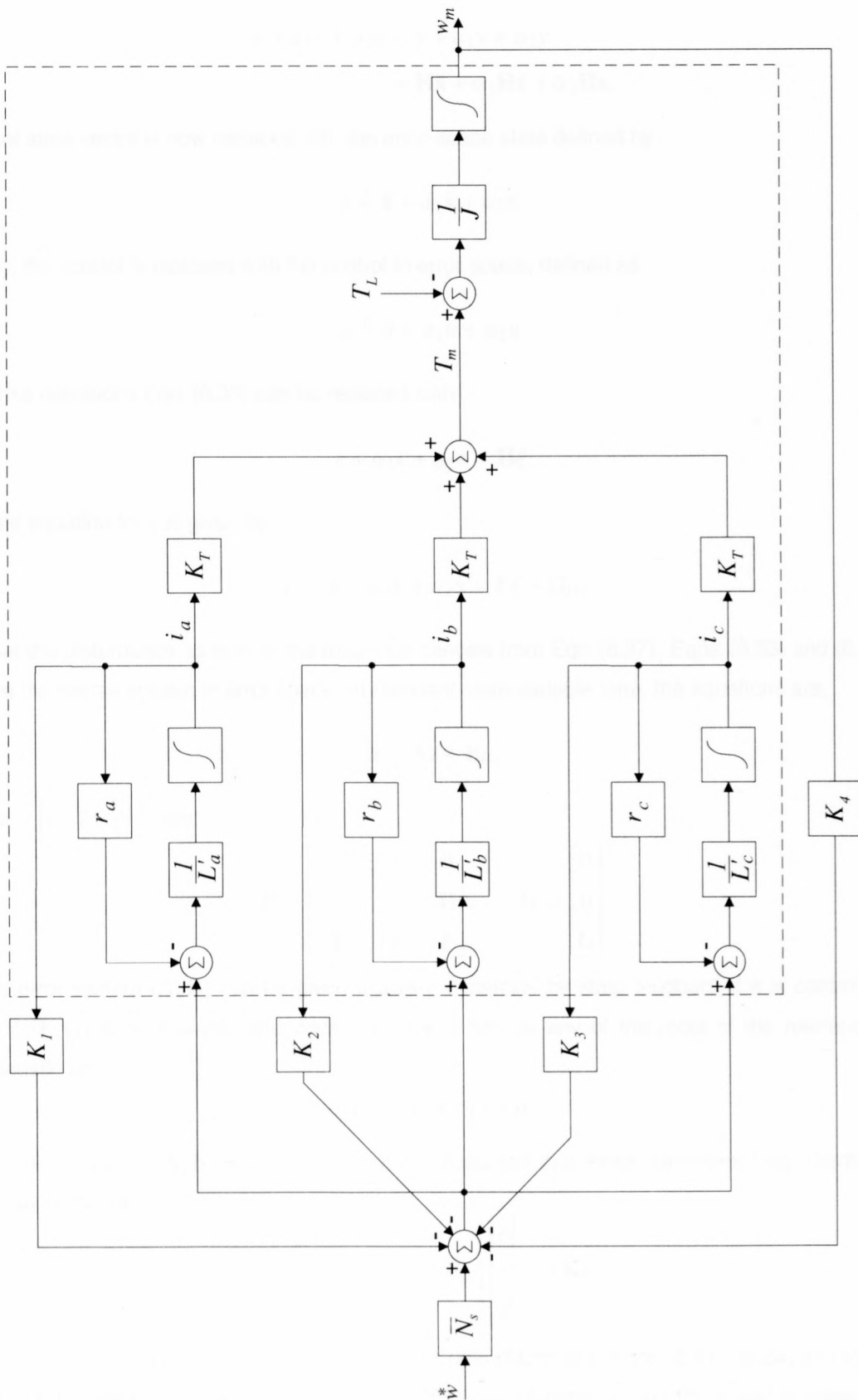


Figure 6.5: Block diagram for simplified speed control of a three phase machine

By substituting r from Eqn. (6.32) into Eqn. (6.30) a formula is obtained for the error in terms of the state,

$$\begin{aligned}\ddot{e} + \alpha_1 \dot{e} + \alpha_2 e &= \ddot{y} + \alpha_1 \dot{y} + \alpha_2 y \\ &= \mathbf{H}\ddot{\mathbf{x}} + \alpha_1 \mathbf{H}\dot{\mathbf{x}} + \alpha_2 \mathbf{H}\mathbf{x}.\end{aligned}\quad (6.33)$$

The plant state vector is now replaced with the error-space state defined by

$$\xi \triangleq \ddot{\mathbf{x}} + \alpha_1 \dot{\mathbf{x}} + \alpha_2 \mathbf{x}.\quad (6.34)$$

Similarly, the control is replaced with the control in error space, defined as

$$\mu \triangleq \ddot{u} + \alpha_1 \dot{u} + \alpha_2 u.\quad (6.35)$$

With these definitions Eqn. (6.33) can be replaced with

$$\ddot{e} + \alpha_1 \dot{e} + \alpha_2 e = \mathbf{H}\xi.\quad (6.36)$$

The state equation for ξ is given by

$$\xi = \ddot{\mathbf{x}} + \alpha_1 \dot{\mathbf{x}} + \alpha_2 \mathbf{x} = \mathbf{F}\xi + \mathbf{G}\mu.\quad (6.37)$$

Note that the disturbance as well as the reference cancels from Eqn. (6.37). Eqns. (6.33) and (6.37) now describe the overall system in error space. In standard state-variable form, the equations are,

$$\dot{\mathbf{z}} = \mathbf{A}\mathbf{z} + \mathbf{B}\mu,\quad (6.38)$$

where $\mathbf{z} = [e \quad \dot{e} \quad \xi^T]^T$ and

$$\mathbf{F} = \begin{bmatrix} 0 & 1 & \mathbf{0} \\ -\alpha_2 & -\alpha_1 & \mathbf{H} \\ \mathbf{0} & \mathbf{0} & \mathbf{F} \end{bmatrix}, \quad \mathbf{G} = \begin{bmatrix} 0 \\ 0 \\ \mathbf{G} \end{bmatrix}.\quad (6.39)$$

The error system (\mathbf{A}, \mathbf{B}) can be given arbitrary dynamics by state feedback if it is controllable. If the plant (\mathbf{F}, \mathbf{G}) is controllable and does not have a zero at any of the roots of the reference-signal characteristic equation

$$\alpha_r(s) = s^2 + \alpha_1 s + \alpha_2,\quad (6.40)$$

then the error system (\mathbf{A}, \mathbf{B}) is controllable. If it is assumed that these conditions hold, there exists a control law of the form

$$\mu = -\begin{bmatrix} K_2 & K_1 & \mathbf{K}_0 \end{bmatrix} \begin{bmatrix} e \\ \dot{e} \\ \xi \end{bmatrix} = -\mathbf{K}\mathbf{z},\quad (6.41)$$

such that the error system has arbitrary dynamics by pole placement. Eqns. (6.41), (6.34) and (6.35) can be combined to obtain the control law in terms of the actual control, u , and the actual process state, \mathbf{x} , ($\frac{d^2 u}{dt^2}$ is written as u''),

$$(u + \mathbf{K}_0 \mathbf{x})'' + \sum_{i=1}^2 \alpha_i (u + \mathbf{K}_0 \mathbf{x})^{(2-i)} = - \sum_{i=1}^2 K_i e^{(2-i)}.\quad (6.42)$$

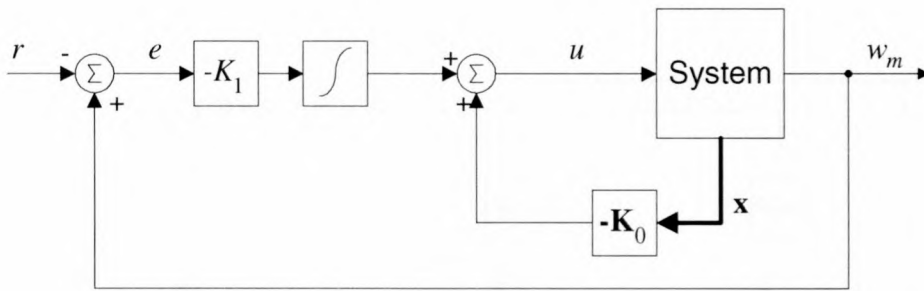


Figure 6.7: Robust control block diagram

In the case where the reference input is a constant, $\dot{r} = 0$, the control law (Eqn. (6.42)), in terms of u and \mathbf{x} reduces to

$$\dot{u} + \mathbf{K}_0 \dot{\mathbf{x}} = -K_1 e. \quad (6.43)$$

By integrating Eqn. (6.43), it is seen that one of the control signal u 's terms contains a pure integrator. Fig. 6.7 [22] shows the block diagram representation of this control approach.

\mathbf{K} is now determined using the LQR method in the same way as previously with the new matrices \mathbf{A} and \mathbf{B} ,

$$K_1 = 1.0, \quad \mathbf{K}_0 = \begin{bmatrix} 0.9724 & 0.9724 & 0.9724 & 1.0014 \end{bmatrix} \quad (6.44)$$

6.5.3 Simulation

Making use of these values the step response with a load was determined by simulation, and is shown in Fig. 6.8. It can be seen that the new control system has a zero steady-state error. The response time is not as good as the previous system, but this could be improved by feeding the error forward [22]. The feedforward can be used to cancel a pole of the system and improve the dynamic response of the system.

6.6 DSP and Machine Effects

This section discusses the potential effects which could arise from the machine parameters that were approximated or not taken into account in the control system design, and the effects of the DSP control system on the accuracy of the control. Simulations are then presented as the various aspects are investigated.

6.6.1 Machine effects

There are a number of effects inherent to the machine that were not taken into account when designing the control system. They are,

1. The torque is a function of both position and current. The control systems were designed making use of the average torque per ampere.

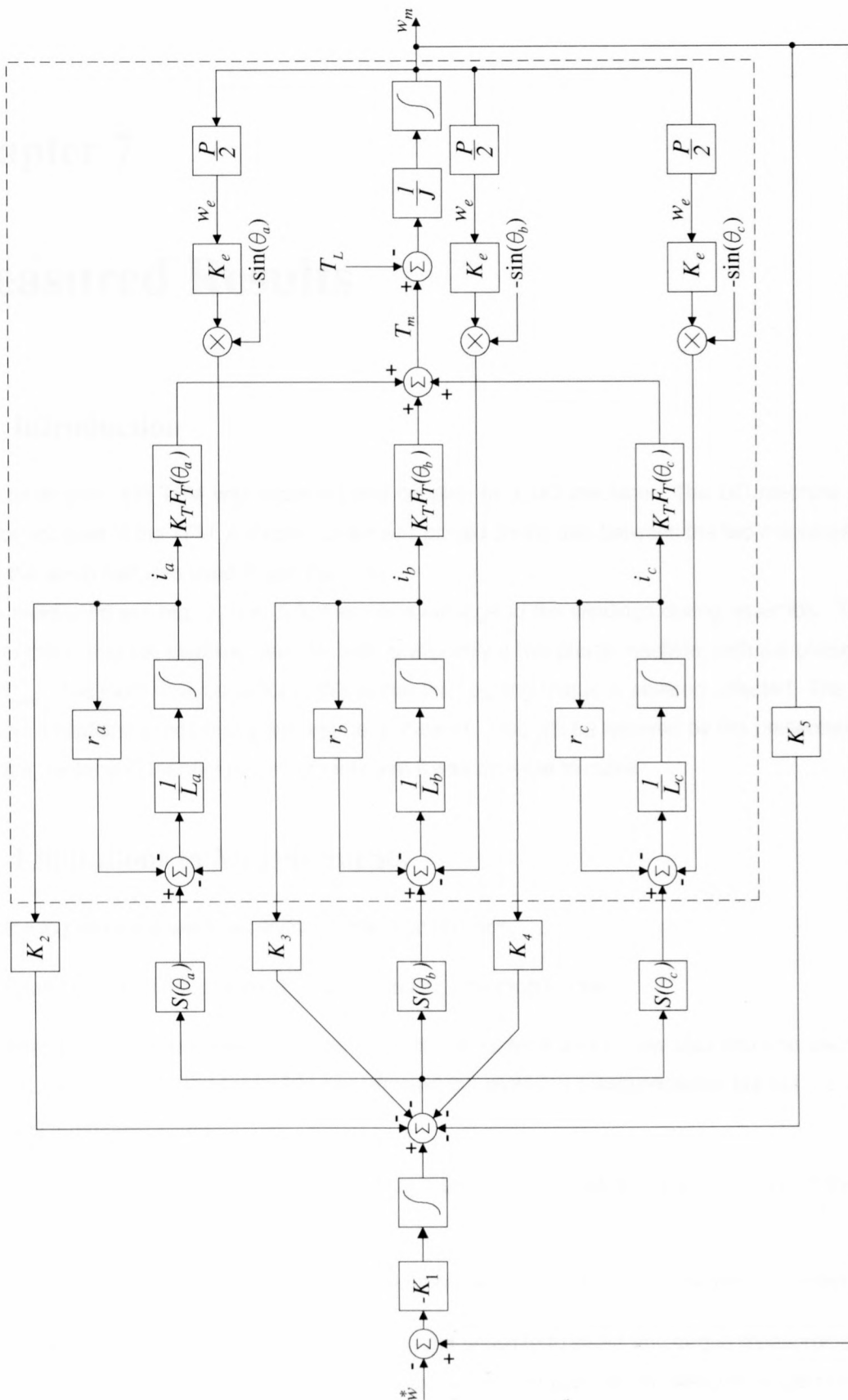


Figure 6.16: Complete block diagram for speed control of a three phase machine

Chapter 7

Measured Results

7.1 Introduction

After construction the TFM was mounted and coupled to a DC machine. The DC machine acted as actuator and load to the TFM. A torque sensor was placed on the axis between the two machines. Fig. 7.1 shows the setup that was used to test the TFM.

As mentioned in Chap. 5, Sec. 5.3, there was damage to the windings during assembly. The major result of this is that the machine used for testing was only a two phase machine, with the phases shifted by $120^{\circ}_{\text{elec}}$. The most obvious effect of this is that the cogging torque is severely affected. The observations and limitations experienced will first be discussed. This will be followed by the presentation of the generator, motor and thermal measurements that it was possible to make.

7.2 Limitations to Measurements

The following problems were experienced after construction,

1. Phase B had an internal short, resulting in large cogging torque.
2. After Phase B was removed, it was found that Phases A and C now also had one short each to the chassis. It is suspected that this affected the motoring measurements, but not the generator measurements.
3. The torque sensor was operational, but then failed. It is suspected that the shorts to the chassis may have resulted in this.
4. Phase C showed erratic behaviour when current was injected into it by the power converter.

As a result of the torque sensor failure, it was not possible to make any torque measurements. This was very unfortunate, as this would have served as the best comparison between the actual machine and the simulations. The erratic behaviour of Phase C meant that it was only possible to stimulate Phase A during attempts to measure the motoring torque.

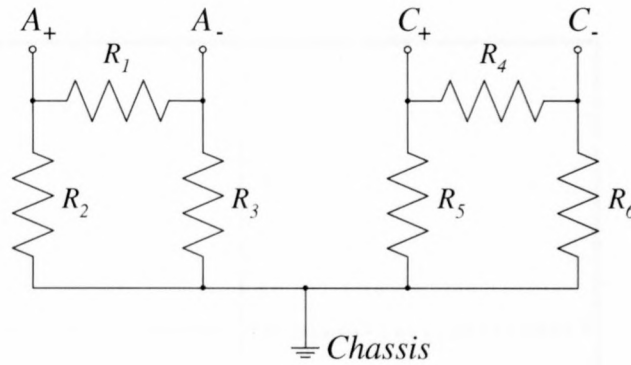


Figure 7.4: Model of the measured winding resistances

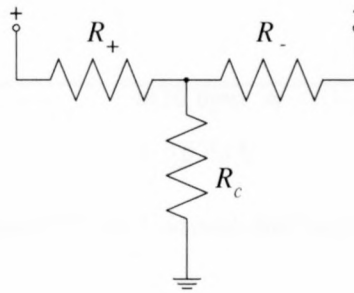


Figure 7.5: Model to determine point of winding damage

determine the resistances as shown in Fig. 7.5. If these resistances are determined, it can be estimated at which point the windings are shorting to the chassis. It is simple to calculate these values and Table 7.2 gives the results. From the values of R_{A+} and R_{B-} , it is reasonable to assume that the damage occurred near the point where the winding terminals enter into the machine. There was most likely an insulation failure at these points as a result of the assembly and disassembly.

As a result of this, it was necessary to take precautions not to connect the two phases together, either directly or through measuring equipment.

Table 7.2: Model winding resistances

	Phase A	Phase B
R_+	12.95m Ω	109.65m Ω
R_-	113.85m Ω	13.65m Ω
R_c	119.15m Ω	211.35.0m Ω

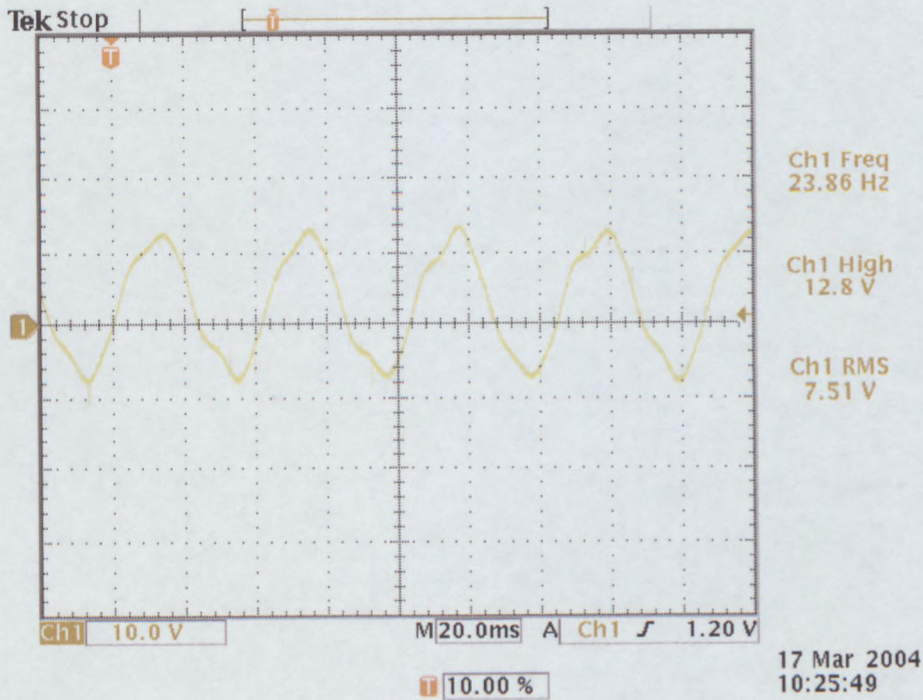


Figure 7.7: No load back EMF at 30 rpm

damaging the machine). Another thing to note is the high frequency in Fig. 7.8. These frequencies are achievable as a result of the isotropic nature of the core material, SMC.

7.3.2 Generator Under Load

A resistor was connected to each of the two phases, and the voltages and currents under load were measured. The measured load resistor values were $R_{LA} = 1.201\Omega$ and $R_{LC} = 1.143\Omega$. Figures 7.9 and 7.10 show scope captures of the voltages and currents at different speeds. There was only one high current probe available, so it was only possible to measure a single phase when the current was above 10 A.

The most interesting things to note are that the current lags the voltage (visible in Fig. 7.10), and that there is a significant voltage drop at the terminals (compared to the no load back EMF). This can be explained by referring to Fig. 3.1 (electrical model of a phase) and Fig. 3.5 (inductance vs. position); from this it can be deduced that there is a significant voltage drop across the inductance of the coil at high frequencies.

7.4 Motor Measurements

Due to time constraints and partially to the faults in the machine it was not possible to implement a working current or speed control system. Some preliminary measurements were made, but no decent results were obtained. It was seen that Phase C did not operate correctly when voltages were applied to it. Instead of

Chapter 8

Conclusions

8.1 Summary

A passive rotor transverse flux machine was designed and built. The machine was designed to have three phases, and output 50 kW. The design was chosen after a number of simulations and a preliminary investigation into the viability of different designs were done. A soft magnetic composite (Somalloy 550, Höganäs AB) was used as the core material and high temperature NeFeB magnets were used. The various topologies investigated include reluctance TFMs, reluctance TFMs with small magnetic shields, active rotor TFMs with and without flux concentration, and four different passive rotor TFMs, namely the C-Core, RMM, I-Core and the U-Core configurations. The process of choosing a configuration is not an easy one as there are more parameters than just the performance, such as the constructibility. Based on a preliminary investigation the U-Core passive rotor design was chosen. The construction of the machine was a complicated process, which was made more difficult by the fact that the SMC components had to be machined from pressed SMC cylinders. After assembly it was found that one phase was not functioning correctly. After removing this phase, the other two phases also experienced electrical problems, but this was not prohibitive to testing. Generator tests were done and it was found that the machine did not perform exactly as expected. It is not known if this was due to simulation errors, or to construction faults in the machine. A control scheme for motoring operation of the machine was designed, but not properly implemented due to time constraints and the speed and accuracy of the DSP system. Open loop motoring tests were done, which also illustrate that the machine can be operated in this mode. Thermal transfer tests were also done and compared to simulations.

The machine did not perform as well as hoped, and it was not possible to make torque measurements due to failure of the torque sensor. Unfortunately construction problems and time constraints meant that a complete set of results was not obtainable.

The passive rotor TFM shows promising results in simulations, but requires more work to determine if this machine is a viable option for commercial use. It would appear that the most promising application of this machine would be as a low speed generator with a high number of phases. The high number of phases would result in low cogging torque, and the low speed would mean that the magnetic losses of the SMC do not play a significant role in the efficiency of the machine. Also, if the machine was only used

as a generator, there would not be a need for a complex motor controller. The complex construction of the machine is, at this point, a large limiting factor to its adoption in industry. The construction challenges would be reduced, but not eliminated, if the correct shape SMC components can be manufactured by pressing and sintering, rather than conventional machining.

8.2 Recommendations

In light of the results, the following recommendations can be made,

- Simulations should be done making use of a rotary model, taking into account the radius of curvature of the components (a solid modeler will have to be purchased to achieve this with Magnet). These simulations should be compared to the linear model simulations.
- An optimisation which attempts to minimize the magnet volume of the U-Core TFM should be done.
- A machine which operates at frequencies that do not cause serious magnetic losses should be investigated.
- The number of windings per coil should be reconsidered to achieve better generator performance.
- A complete set of torque measurements should be obtained for the constructed machine to compare to the simulations.
- If another machine of this type is constructed the following should be done,
 1. The SMC components should be pressed and sintered by a metal powder manufacturer.
 2. An external rotor motor should be considered. This could result in easier insertion of the coils (this could be done after casting), a higher output torque, and less centrifugal strain on the rotor SMC blocks.
 3. The construction should be done in such a way that if a phase fails, it can be relatively easily replaced (this was possible with the stator of the machine presented, the rotor could be examined too, but due to its passive nature has a lower potential of failure).
- Further investigations into the heat transfer of the machine should be done.
- Simulations should be done to confirm the results from the generator tests.
- An investigation into the use of the rotating reference frame variables for the design of the control system should be done.

It is the author's opinion that a 5-phase, low speed wind generator, with an operating frequency below 500 Hz, and an external rotor be investigated. Making use of 5-phases would result in a low cogging torque. The cogging torque could be minimised by making use of slightly more complex geometrical shapes, and rotor skew. A metal powder manufacturer should press and sinter the components for this machine.

8.3 Conclusions

The transverse flux machine is a complex machine with many possible applications. Currently the main obstacles facing this machine are the complexity of its construction, limitations of the suitable materials available for construction, and the expensive tools needed to design the machine (3D finite element analysis packages). All of these result in a very high cost machine. To make the machine appealing to industry, the cost versus benefit would have to be greatly improved. Insight into the construction methods was obtained in this investigation, and some relevant recommendations made above. To further the adoption of this type of machine, more support is needed from the relevant industrial partners, namely SMC powder and component manufacturers.

References

- [1] H. Weh, H. Hoffman, and J. Landrath, "New permanent magnet excited synchronous machine with high efficiency at low speeds," *Int. Conf. on Electrical Machines*, vol. 3, pp. 35–40, 1988, Pisa.
- [2] H. Weh, "Transverse flux machines in drive and generator application," *Proc. Stockholm Power Tech Conference*, pp. 75–80, June 1995.
- [3] G. D'Angelo, R. Di Stefano, and M. Scarano, "A TF PM motor wheel drive: Test and experimental results," *Proc. Int. Conf. on Electrical Machines (ICEM)*, vol. 2, pp. 179–183, 1996, Vigo, Spain.
- [4] M. Bork and G. Henneberger, "New transverse flux concept for an electric vehicle drive system," *Proc. Int. Conf. on Electrical Machines (ICEM)*, vol. 2, pp. 308–313, 1996, Vigo, Spain.
- [5] R. Blissenbach and G. Henneberger, "Transverse flux motor with high specific torque and efficiency for a direct drive of an electrical vehicle," *Proc. ISATA (Clean Power Sources and Environmental Implications in the Automotive Industry)*, pp. 429–436, 1999, Vienna, Austria.
- [6] R. Blissenbach and G. Henneberger, "New design of a transverse flux machine for a wheel hub motor in a tram," *Proc. PCIM (Intelligent Motion)*, pp. 189–194, 1999, Nuremberg, Germany.
- [7] R. Blissenbach and G. Henneberger, "Development of a transverse flux traction motor in a direct drive system," *Proc. Int. Conf. on Electrical Machines (ICEM)*, vol. 3, pp. 1457–1460, 2000, Helsinki, Finland.
- [8] R. Blissenbach and G. Henneberger, "New design of a soft magnetic composite transverse flux machine with special attention on the loss mechanisms," *Proc. Electromotion*, June 2001, Bologna, Italy.
- [9] B.C. Mecrow, A.G. Jack, and C.P. Maddison, "Permanent magnet machines for high torque, low speed applications," *Proc. Int. Conf. on Electrical Machines (ICEM)*, vol. 2, pp. 461–466, 1996, Vigo, Spain.
- [10] C.P. Maddison, B.C. Mecrow, and A.G. Jack, "Claw pole geometries for high performance transverse flux machines," *Proc. Int. Conf. on Electrical Machines (ICEM)*, vol. 1, pp. 340–345, 1998, Istanbul, Turkey.
- [11] S.M. Husband and C.G. Hodge, "The Rolls-Royce transverse flux motor development," *IEEE International Electric Machines and Drives Conference*, vol. 3, pp. 1435–1440, June 2003.

-
- [12] B.E. Hasubek, *Analysis and design of passive rotor transverse flux machines with permanent magnets on stator*, Ph.D dissertation, University of Calgary, <http://home.t-online.de/home/hasubek/>, March 2000.
- [13] H. Weh, "Synchronous machines with new topologies," *SM100: Int. Conf. on the Evolution and Modern Aspects of Synchronous Machines*, vol. Part 2, pp. C1–C9, 1991, Zurich.
- [14] P. Jansson, M. Persson, A.G. Jack, and B.C. Mecrow, "Composites pave the way to the electrical machine designs of the future," *Internal report between Höganäs AB, and University of Newcastle Ipon Tyne*.
- [15] A.G. Jack, "Experience with the use of soft magnetic composites in electrical machines," *Proc. Int. Conference on Electrical Machines (ICEM)*, vol. 3, pp. 1441–1448, 1998, Istanbul, Turkey.
- [16] A.G. Jack, B.C. Mecrow, P.G. Dickinson, D. Stephenson, J.S. Burdess, N. Fawcett, and J.T. Evans, "Permanent-magnet machines with powdered iron cores and prepressed windings," *IEEE Trans. Ind. Applicat.*, vol. 36, pp. 1077–1084, July/August 2000.
- [17] R. Blissenbach and G. Henneberger, "Numerical calculation of 3d eddy current fields in transverse flux machines with time stepping procedures," *Int. Journal for Computation and Mathematics in Electrical and Electronic Engineering (COMPEL)*, vol. 20, no. 1, pp. 152–166, 2001.
- [18] R. Kruse, G. Pfaff, and C. Pfeiffer, "Transverse flux reluctance motor for direct servodrive applications," *IEEE Industry Applications Conference*, vol. 1, pp. 655–662, October 1998.
- [19] M. J. Kamper, *Design optimisation of a cageless flux barrier rotor reluctance synchronous machine*, Ph.D dissertation, University of Stellenbosch, December 1996.
- [20] Fitzgerald, *Analysis of electric machinery*, McGraw-Hill, 1984.
- [21] M. Bork, R. Blissenbach, and G. Henneberger, "Identification of the loss distribution in a transverse flux machine," *Proc. Int. Conf. on Electrical Machines (ICEM)*, vol. 3, pp. 1826–1831, 1998, Istanbul, Turkey.
- [22] Gene F. Franklin, J. David Powell, and Abbas Emami-Naeini, *Feedback control of dynamic systems*, Addison-Wesley Publishing Company, Third edition, 1994.

A.1. Sonalloy 550 DataSheet

Appendix A

Magnetic Data

A.1 Somalloy 550 Datasheet

SOFT MAGNETIC COMPOSITES FROM HÖGANÄS METAL POWDERS

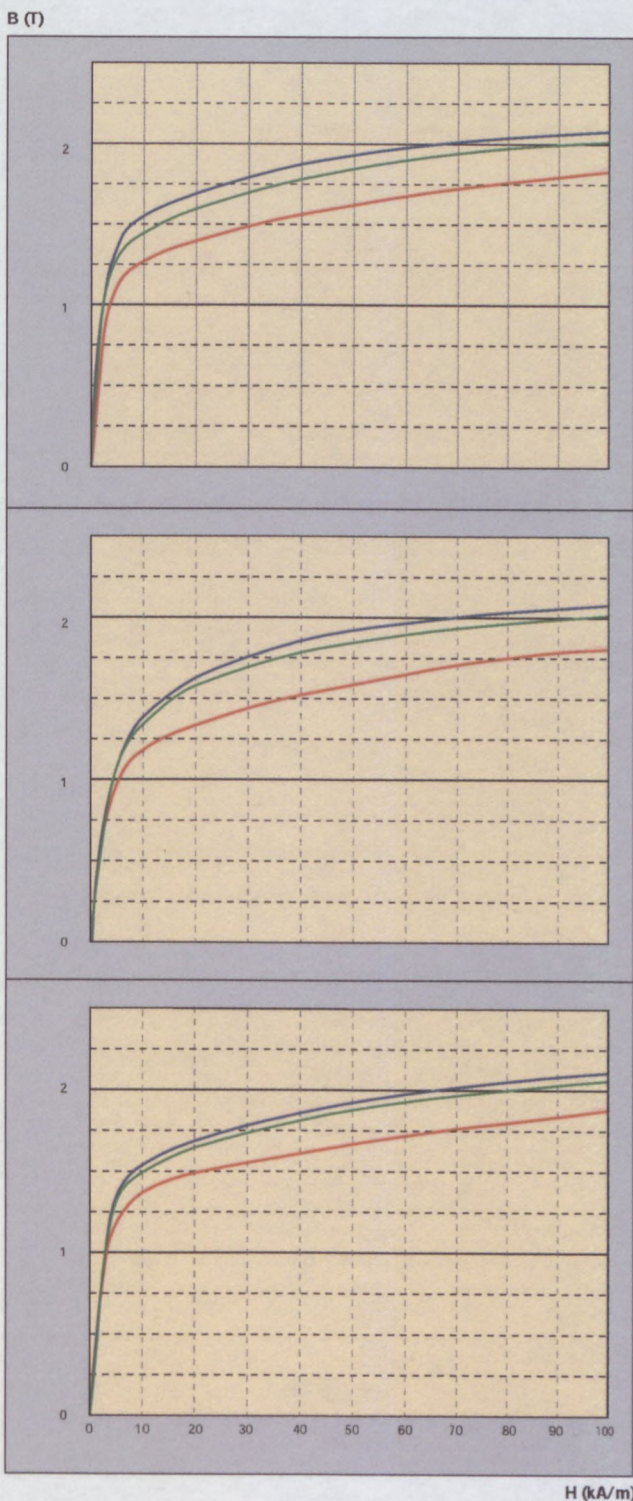
SOMALOY™ 550

SMC 99-1

Höganäs 

SOMALOY™ 550

Typical B-H curves



Premix 1
Somaloy 550 + 0.5% Kenolube
Heat treatment 500°C, 30 min air

7.34 g/cm³

7.20 g/cm³

6.83 g/cm³

Premix 2
Somaloy 550 + 0.6% LB1
Conventional Compaction
Heat treatment 275°C, 60 min air

7.31 g/cm³

7.15 g/cm³

6.73 g/cm³

Premix 2
Somaloy 550 + 0.6% LB1
Warm Compaction
Heat treatment 275°C, 60 min air

7.35 g/cm²

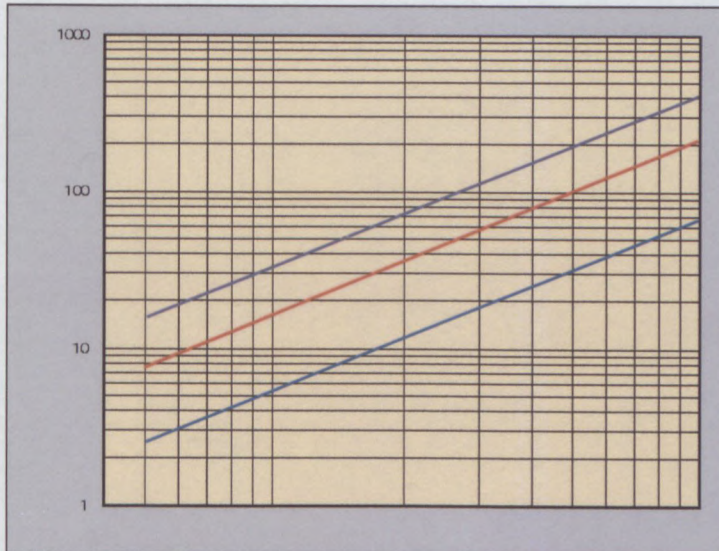
7.28 g/cm²

6.97 g/cm²



Core loss (frequency)

W/kg

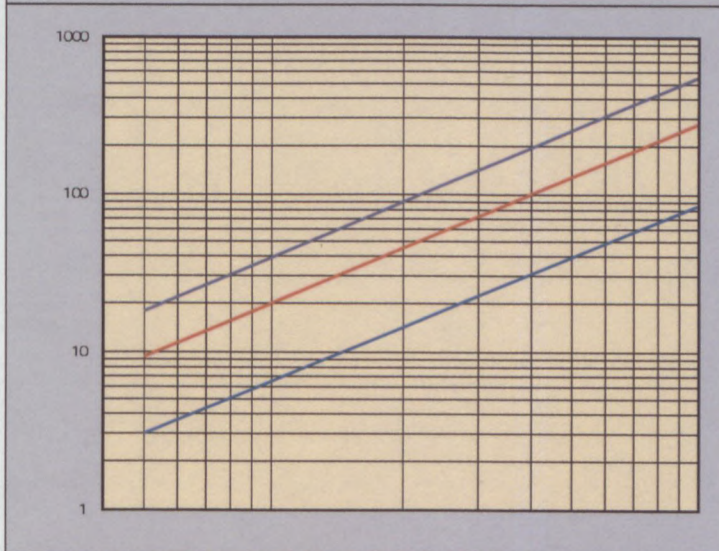


Premix 1
Somaloy 550 + 0.5% Kenolube
Compacting Pressure 800 MPa
Heat treatment 500°C, 30 min air

1.5 T

1.0 T

0.5 T

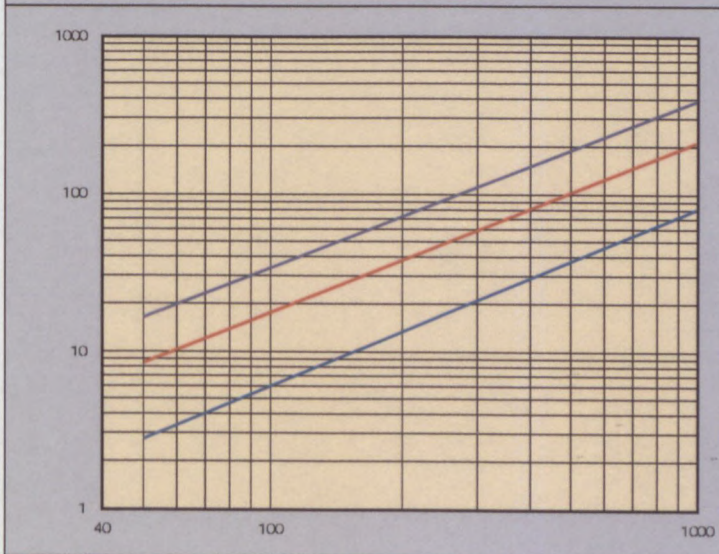


Premix 2
Somaloy 550 + 0.6% LB1
Compacting Pressure 800 MPa
Conventional Compaction
Heat treatment 275°C, 60 min air

1.5 T

1.0 T

0.5 T



Premix 2
Somaloy 550 + 0.6% LB1
Compacting Pressure 800 MPa
Warm Compaction
Heat treatment 275°C, 60 min air

1.5 T

1.0 T

0.5 T

Frequency (Hz)



Physical Properties

POWDER DATA

	Premix 1	Premix 2
AD (g/cm ³)	3,05	3,13
Flow s/50g	34	31

COMPRESSIBILITY (g/cm³)

Compacting pressure (MPa)	400	600	800
Premix 1	6,83	7,23	7,39
Premix 2	6,76	7,15	7,31
Conventional Compaction			
Premix 2	6,88	7,22	7,36
Warm Compaction			

GREEN STRENGTH (GS) MPa

Compacting pressure (MPa)	400	600	800
Premix 1	9,43	14,7	17,1
Premix 2	15,1	21,7	24,3
Conventional Compaction			
Premix 2	14,3	21,0	24,0
Warm Compaction			

Test Conditions

Physical properties were determined in accordance with applicable ISO standards.

Magnetic properties were measured on toroids with the following dimensions:

	Conventionally Compacted	Warm Compacted
Outer diameter	55 mm	40 mm
Inner diameter	45 mm	31 mm
Height	5 mm	5 mm

AFTER HEAT TREATMENT

Physical properties

Premix 1

Somaloy 550 + 0,5% Kenolube

Heat treatment 500° C, 30 min air

Compacting pressure (MPa)	400	600	800
Strength (TRS) MPa	60	50	40
Density (g/cm ³)	6,83	7,20	7,34
Dim. change (%)	-0,003	-0,015	-0,016
μmax	500	550	550

Premix 2

Somaloy 550 + 0,6% LB1

Conventional compaction

Heat treatment 275° C, 60 min air

Compacting pressure (MPa)	400	600	800
Strength (TRS) MPa	75	80	80
Density (g/cm ³)	6,73	7,15	7,31
Dim. change (%)	+0,01	+0,02	+0,05
μmax	200	250	250

Premix 2

Somaloy 550 + 0,6% LB1

Warm compaction

Heat treatment 275° C, 60 min air

Compacting pressure (MPa)	400	600	800
Strength (TRS) MPa	90	100	100
Density (g/cm ³)	6,97	7,28	7,35
Dim. change (%)	-	+0,01	+0,05
μmax	350	350	350

Höganäs

THE DIFFERENCE IS KNOWLEDGE

Höganäs AB (publ), S-263 83 Höganäs, Sweden
Tel. +46 42 33 80 00, Fax +46 42 33 81 50, www.hoganas.com

A.2 Somalloy 500 BH Curve

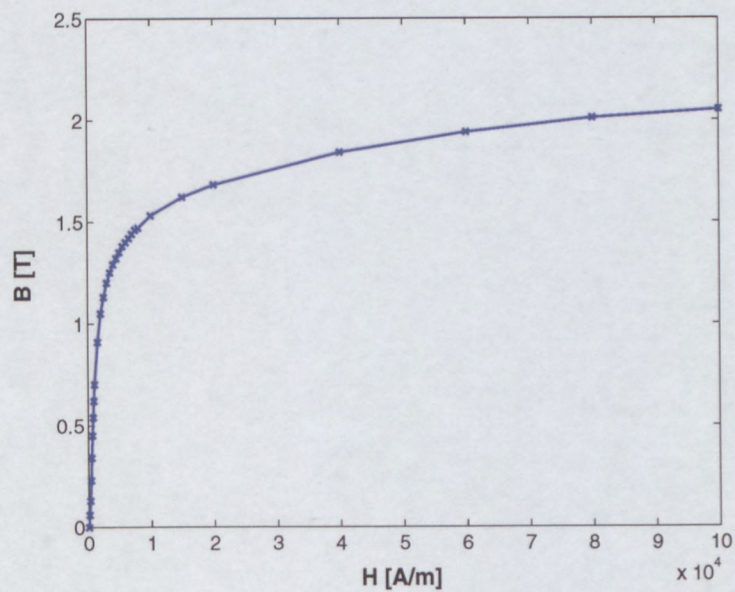


Figure A.1: Somalloy 500 BH Curve

Table A.1: *BH Data for Somalloy 500*

B [T]	H [A/m]
0	0
125	0.06
250	0.13
375	0.23
500	0.34
625	0.45
750	0.54
875	0.62
1000	0.7
1500	0.91
2000	1.05
2500	1.13
3000	1.2
3500	1.25
4000	1.29
4500	1.32
5000	1.35
5500	1.38
6000	1.4
6500	1.42
7000	1.44
7500	1.46
8000	1.47
10000	1.53
15000	1.62
20000	1.84
60000	1.94

Appendix B

Mechanical Drawings

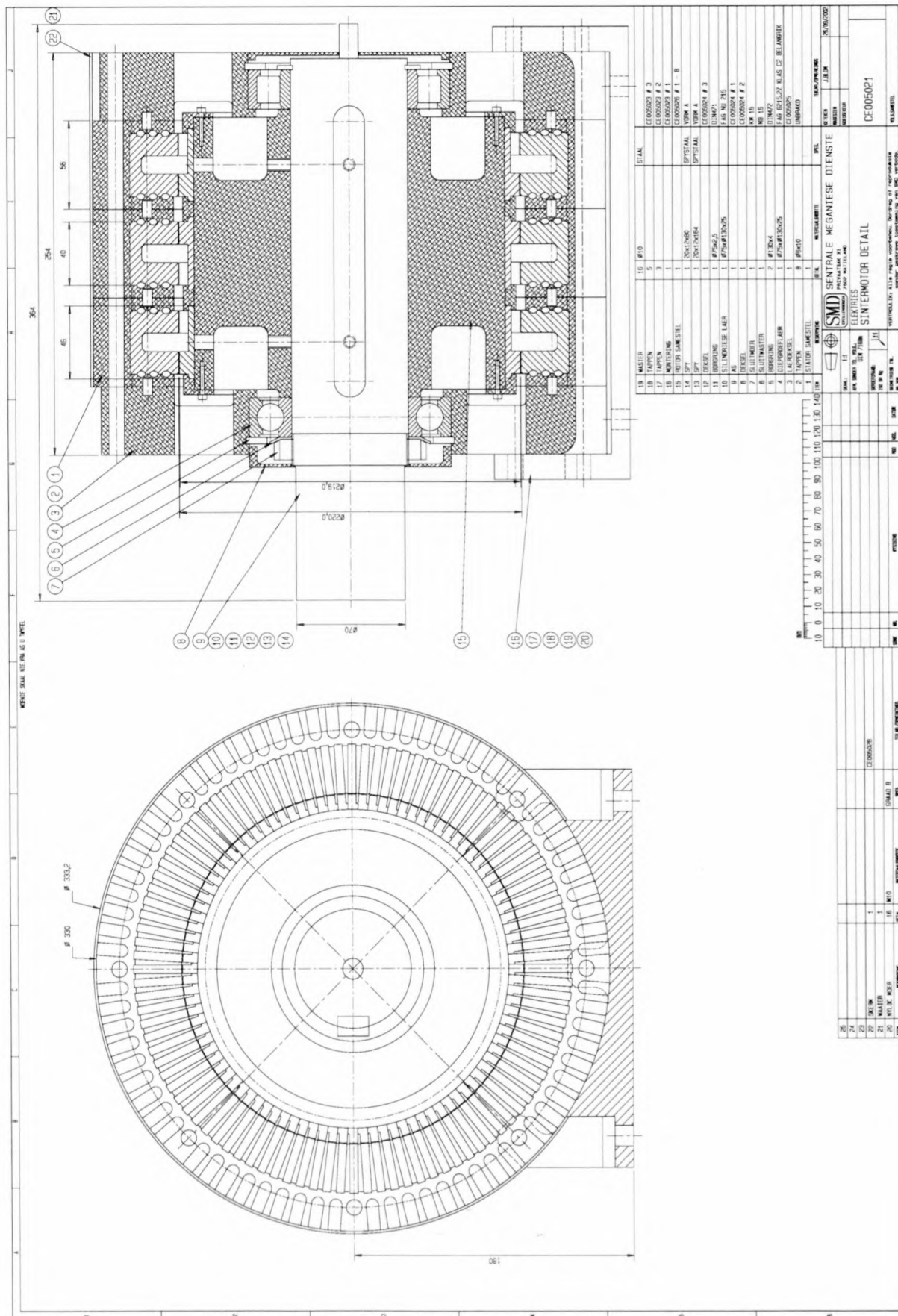


Figure B.1: Complete Machine

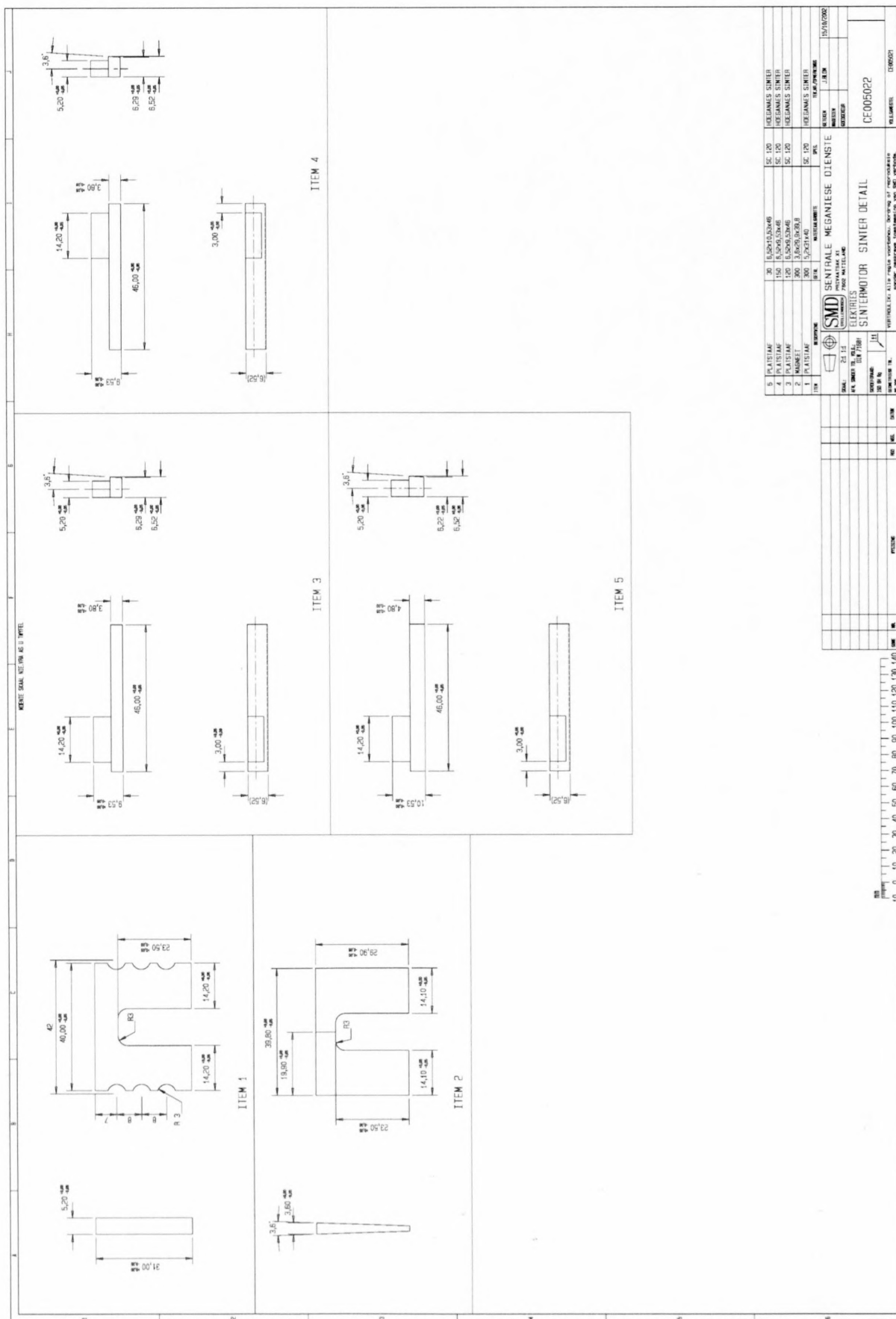


Figure B.2: Machine Components

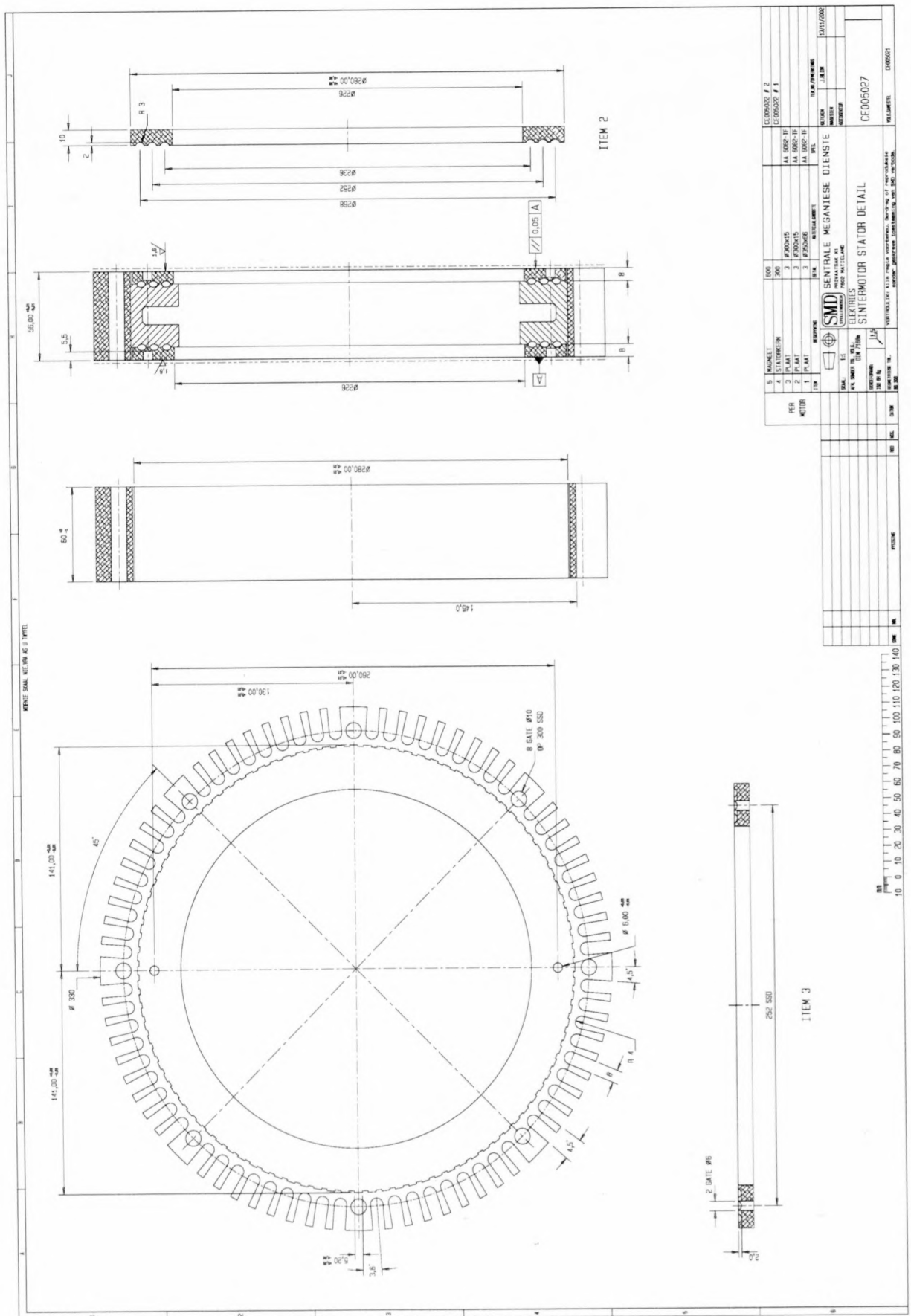


Figure B.3: One Phase

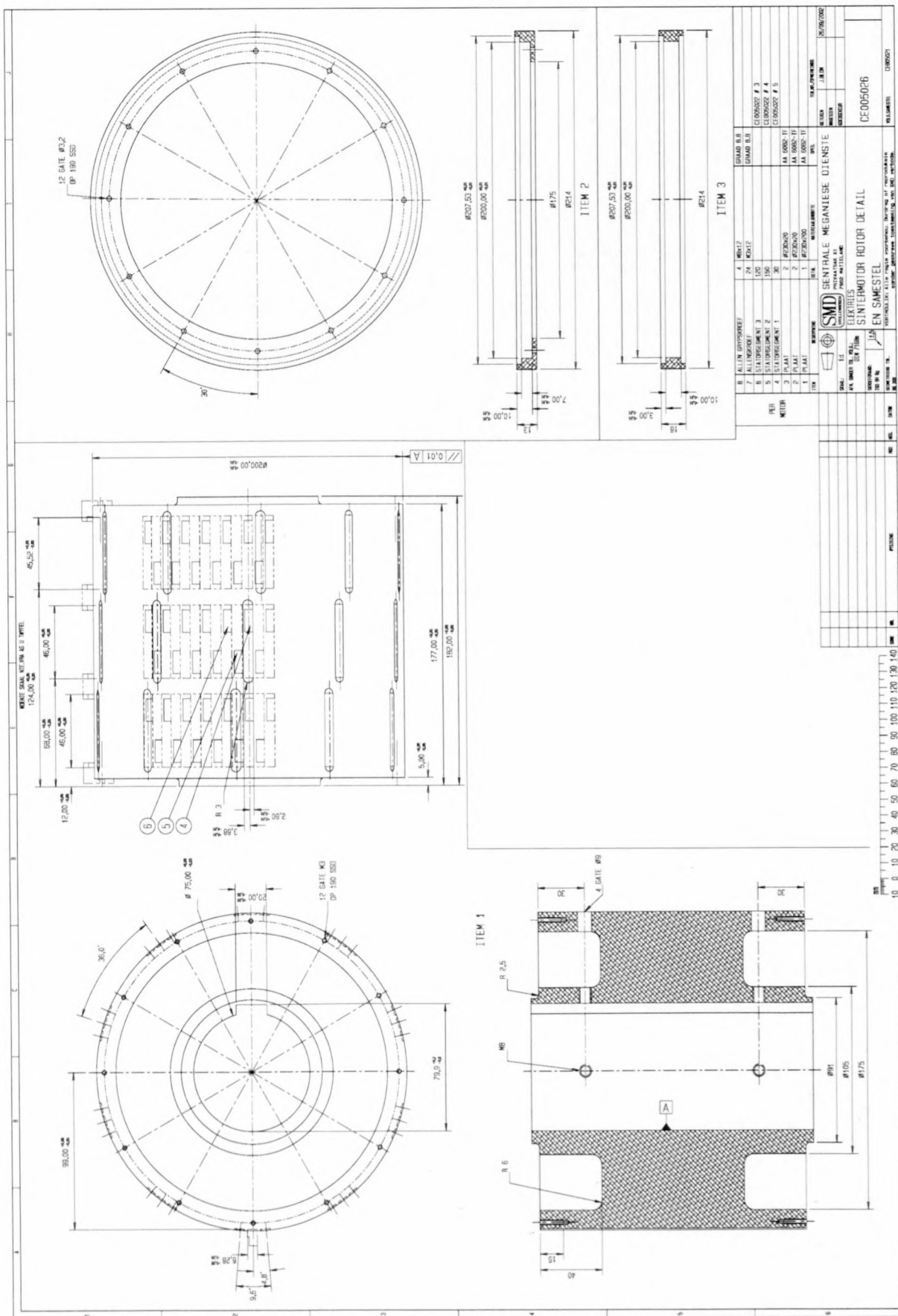


Figure B.4: Rotor

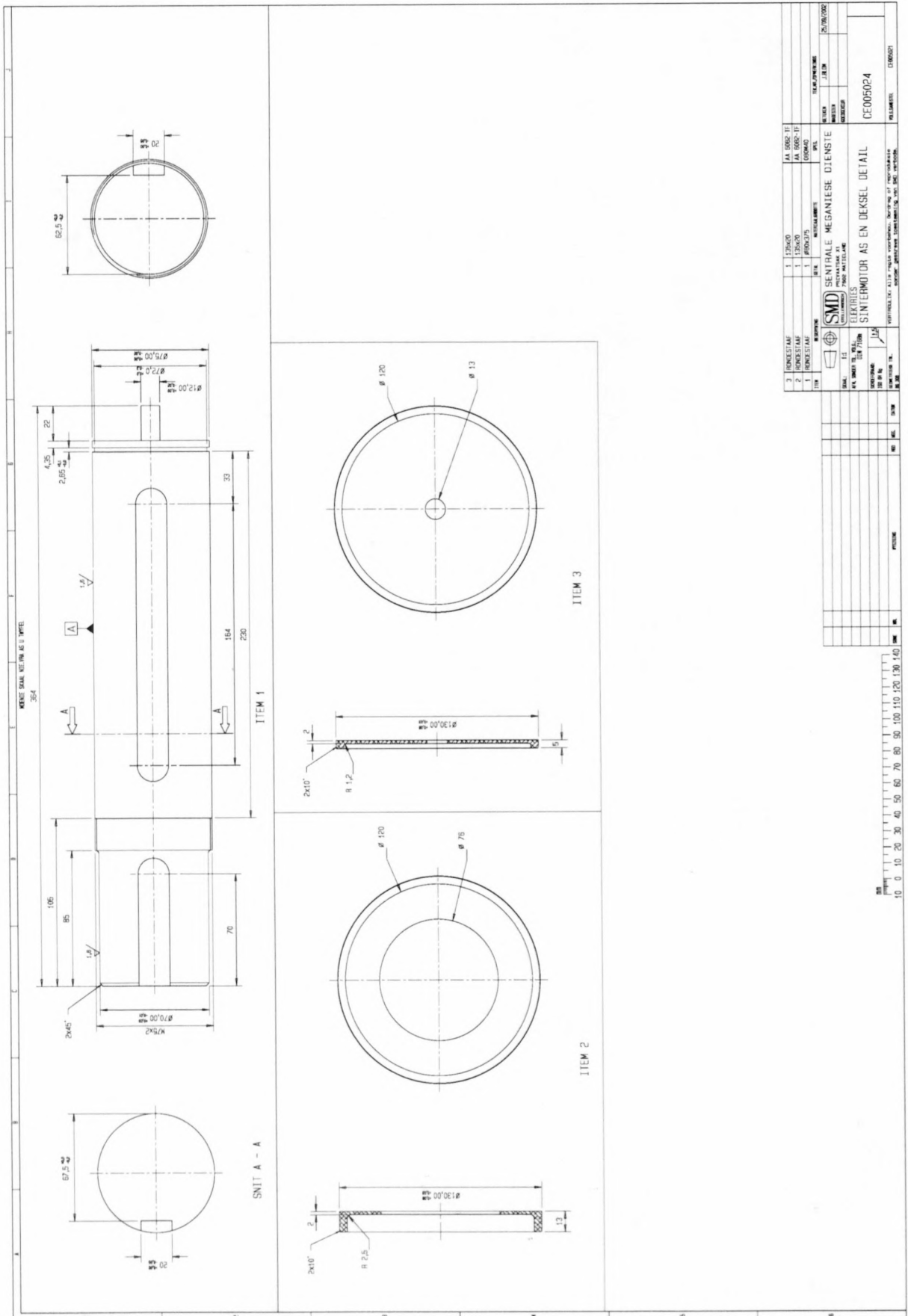


Figure B.5: Shaft

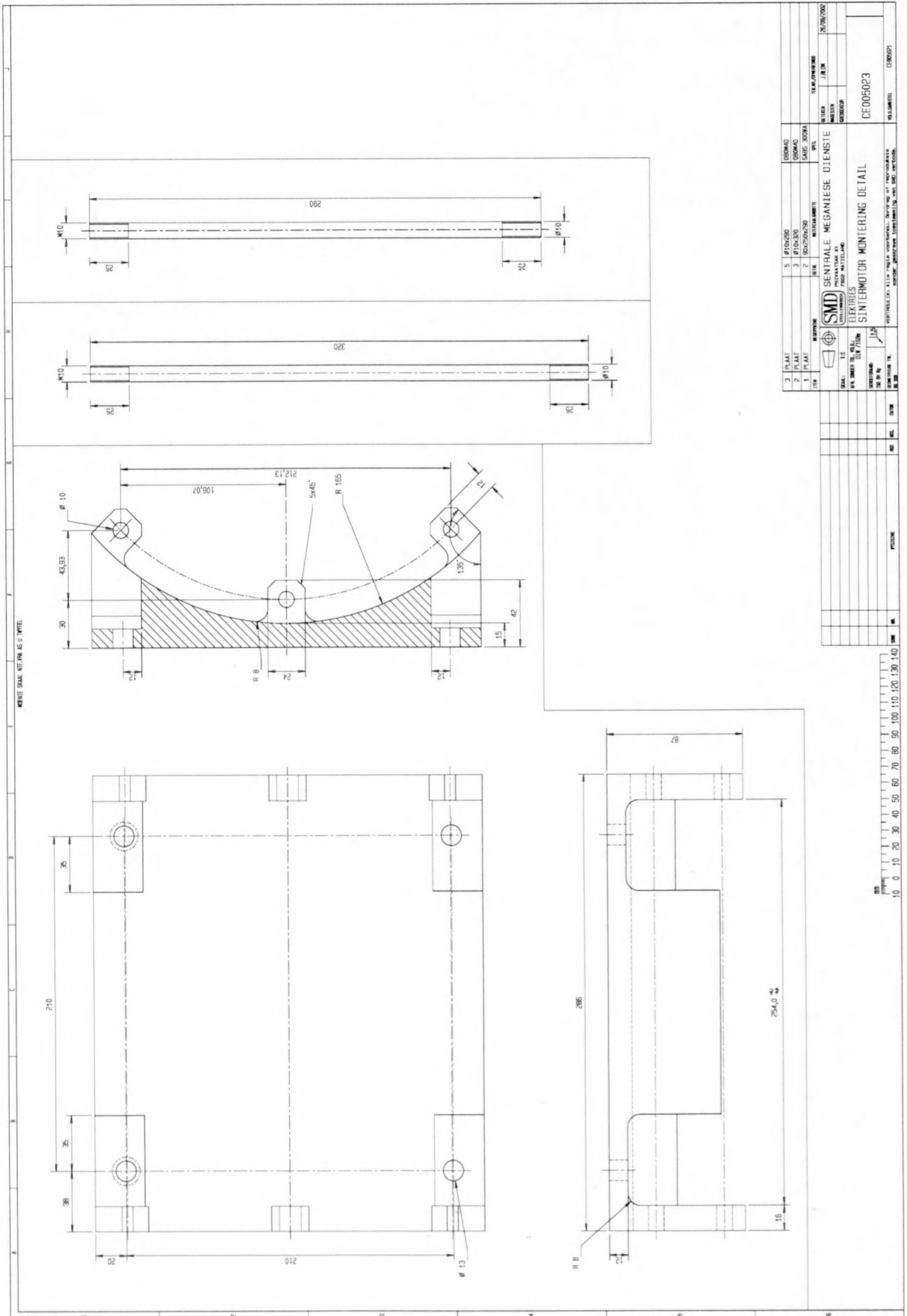


Figure B.7: Mounting

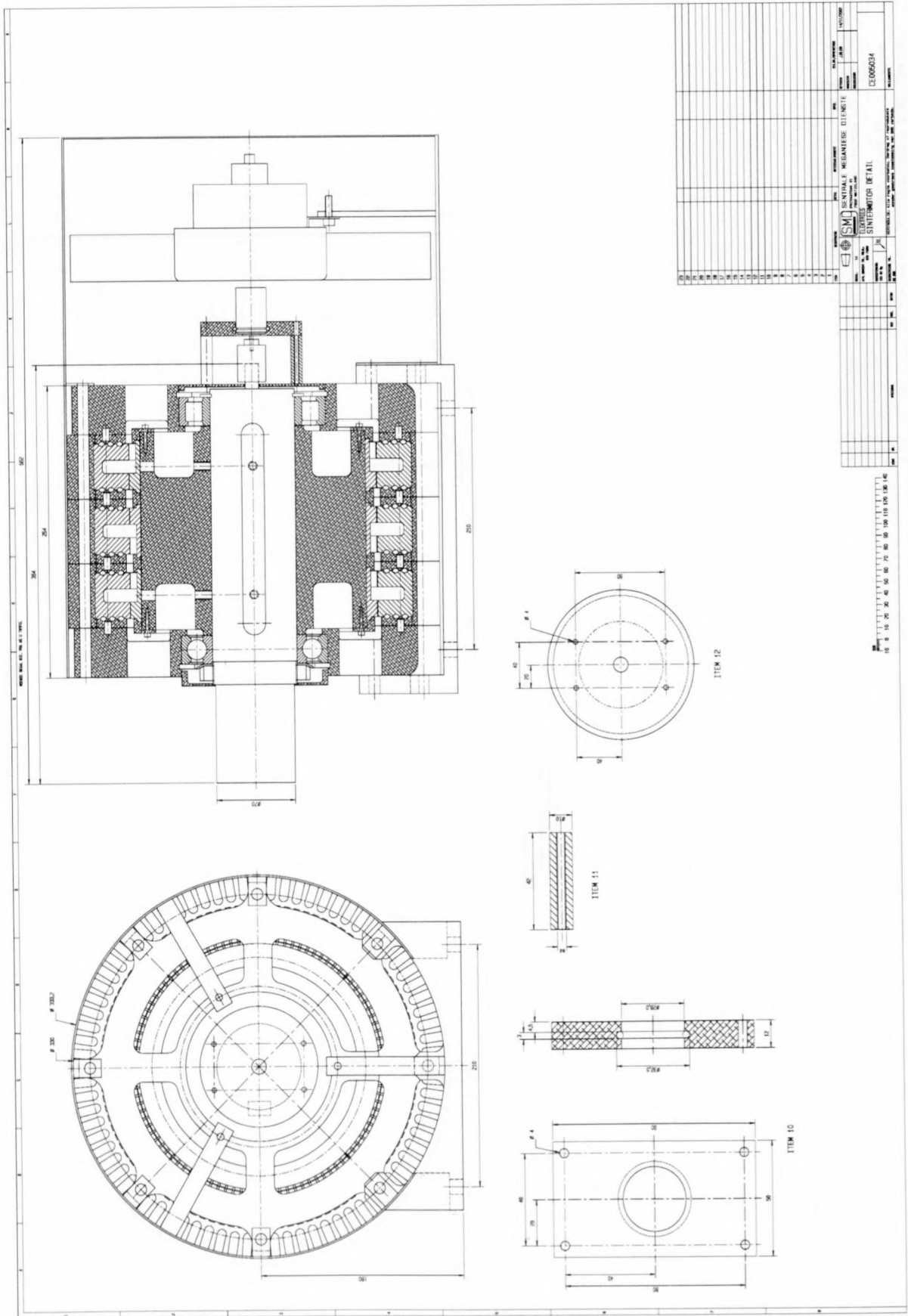


Figure B.8: Fan and Resolver Plate

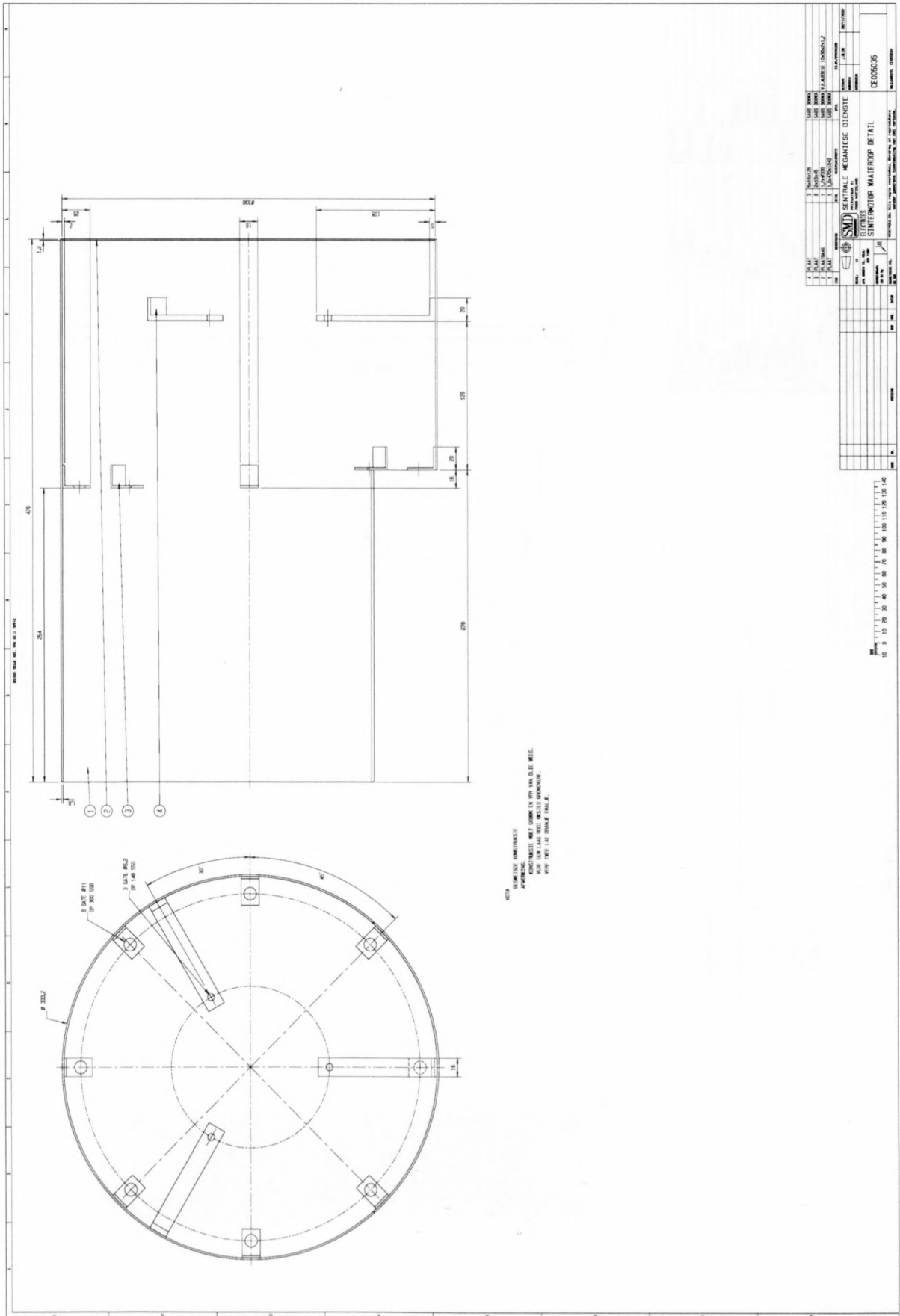


Figure B.9: Fan Housing

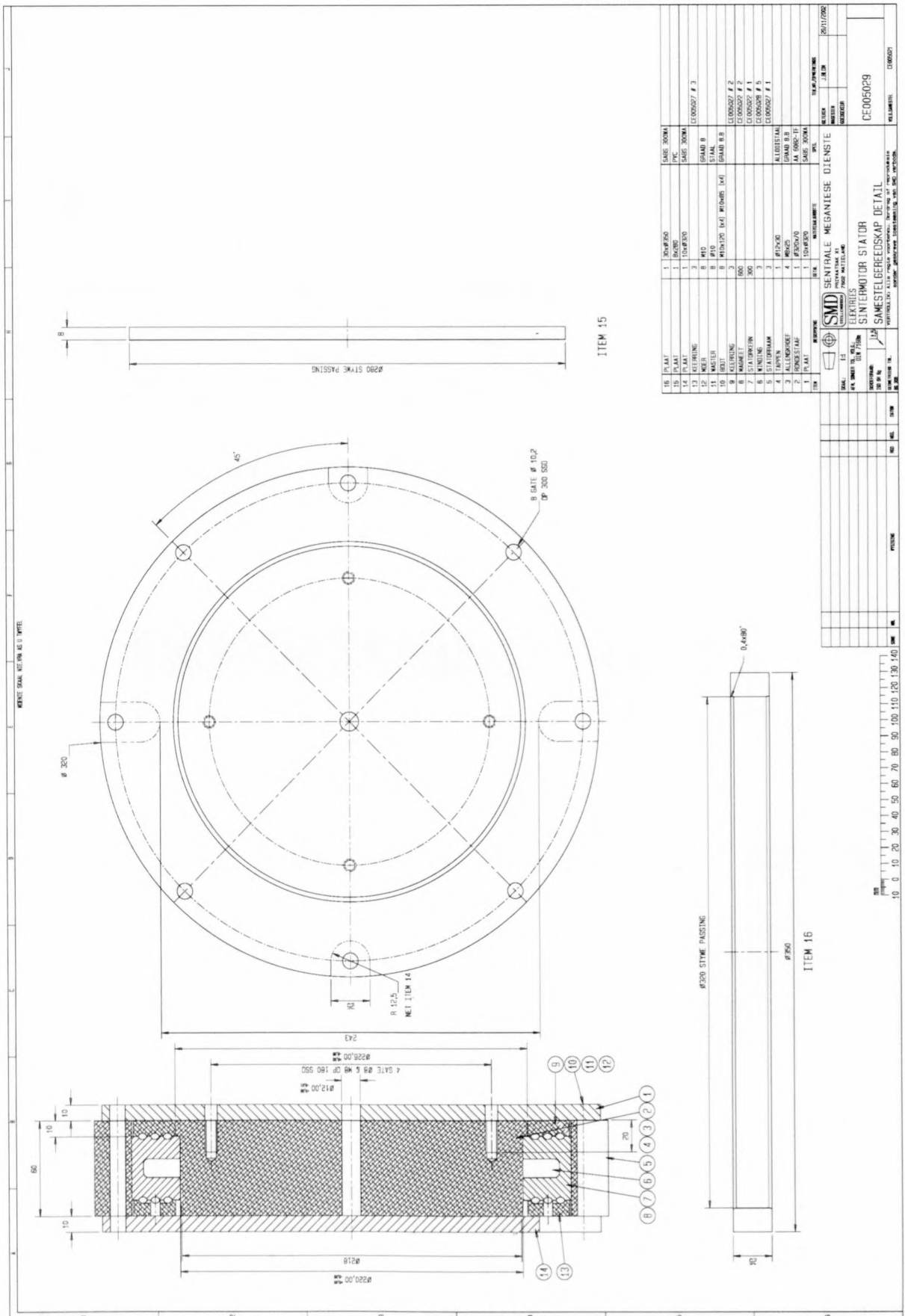


Figure B.10: Stator Mould

Appendix C

Attached CD

C.1 Magnetic Data

Datasheets for both Somalloy 500 and Somalloy 550, and BH curve information for Somalloy 500.

C.2 Magnet Scripts

Scripts used to generate models for Magnet and to optimise model dimensions.

C.3 FE Simulation Data

Output data from relevant Magnet FE simulations.

C.4 Mechanical Drawings

Full set of mechanical drawings (also see Appendix B).

C.5 Photos

Various photos of the machine.

C.6 Control System Simulation Code

C code used to simulate the control system.

C.7 Control System Simulation Results

Results from various control system simulations done with the C program.

C.8 DSP Programs

Control system programs for the DSP controller.

C.9 Raw Measurement Data

Unprocessed measurement data.

C.10 M-files and Simulink Models

Various M-files and simulink models used to generate and process data.